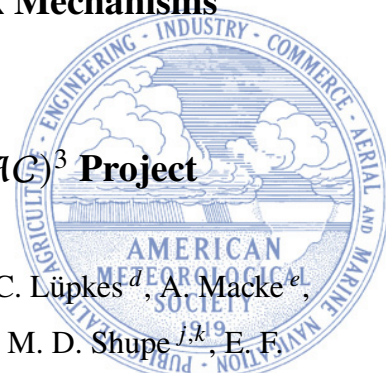


Atmospheric and Surface Processes, and Feedback Mechanisms

Determining Arctic Amplification:

A Review of First Results and Prospects of the (AC)³ Project



Wendisch, M.^a, M. Brückner^a, S. Crewell^b, A. Ehrlich^a, J. Notholt^c, C. Lüpkes^d, A. Macke^e,
J. P. Burrows^c, A. Rinke^d, J. Quaas^a, M. Maturilli^d, V. Schemann^b, M. D. Shupe^{j,k}, E. F.
Akansu^e, C. Barrientos-Velasco^e, K. Bärfuss^l, A.-M. Blechschmidt^c, K. Block^a, I. Bougoudis^c,
H. Bozem^f, C. Böckmann^{d,m}, A. Bracher^{d,c}, H. Bresson^{d,w}, L. Bretschneider^l, M.
Buschmann^c, D. G. Chechin^{d,z}, J. Chylik^b, S. Dahlke^d, H. Deneke^e, K. Dethloff^d, T. Donth^a,
W. Dorn^d, R. Dupuy^g, K. Ebell^b, U. Egerer^{e,x}, R. Engelmann^e, O. Eppers^{f,i}, R. Gerdes^d, R.
Gierens^b, I. V. Gorodetskaya^r, M. Gottschalk^a, H. Griesche^e, V. M. Gryanik^{d,z}, D. Handorf^d,
B. Harm-Altstädter^l, J. Hartmann^d, M. Hartmann^{e,y}, B. Heinold^e, A. Herber^d, H. Herrmann^e,
G. Heygster^c, I. Höschel^d, Z. Hofmann^d, J. Hölemann^d, A. Hünenbein^e, S. Jafariserajehlou^c, E.
Jäkel^a, C. Jacobi^a, M. Janout^d, F. Jansen^s, O. Jourdan^g, Z. Jurányi^d, H. Kalesse-Los^a, T.
Kanzow^d, R. Käthner^l, L. L. Kliesch^b, M. Klingebiel^a, E. M. Knudsen^b, T. Kovács^p, W.
Körtke^c, D. Krampe^d, J. Kretzschmar^a, D. Kreyling^d, B. Kulla^b, D. Kunkel^f, A. Lampert^l, M.
Lauer^b, L. Lelli^{c,u}, A. von Lerber^o, O. Linke^a, U. Löhnert^b, M. Lonardi^a, S. N. Losa^{d,v}, M.
Losch^d, M. Maahn^a, M. Mech^b, L. Mei^c, S. Mertes^e, E. Metzner^a, D. Mewes^a, J. Michaelis^d,
G. Mioche^g, M. Moser^{q,f}, K. Nakoudi^d, R. Neggers^b, R. Neuber^d, T. Nomokonova^b, J.
Oelker^{c,d}, I. Papakonstantinou-Presvelou^a, F. Pätzold^l, V. Pefanis^{c,d}, C. Pohl^c, M. van
Pinxteren^e, A. Radovan^b, M. Rhein^c, M. Rex^d, A. Richter^c, N. Risse^b, C. Ritter^d, P.
Rostosky^c, V. V. Rozanov^c, E. Ruiz Donoso^a, P. Saavedra-Garfias^a, M. Salzmann^a, J. Schacht^e,
M. Schäfer^a, J. Schneiderⁱ, N. Schnierstein^b, P. Seifert^e, S. Seo^c, H. Siebert^e, M. A. Soppa^d, G.
Spreeen^c, I. S. Stachlewska^t, J. Stapf^a, F. Stratmann^e, I. Tegen^e, C. Viceto^r, C. Voigt^{q,f}, M.
Vountas^c, A. Walbröl^b, M. Walter^c, B. Wehner^e, H. Wex^e, S. Willmesⁿ, M. Zanatta^d, and S.
Zeppenfeld^e

Early Online Release: This preliminary version has been accepted for publication in *Bulletin of the American Meteorological Society*, may be fully cited, and has been assigned DOI 10.1175/BAMS-D-21-0218.1. The final typeset copyedited article will replace the EOR at the above DOI when it is published.

^a*Leipziger Institut für Meteorologie (LIM), Universität Leipzig, Deutschland*

^b*Institut für Geophysik und Meteorologie (IGM), Universität zu Köln, Deutschland*

^c*Institut für Umweltphysik (IUP), Universität Bremen, Deutschland*

^d*Alfred–Wegener–Institut, Helmholtz–Zentrum für Polar– und Meeresforschung (AWI),
Bremerhaven & Potsdam, Deutschland*

^e*Leibniz–Institut für Troposphärenforschung (TROPOS), Leipzig, Deutschland*

^f*Institut für Physik der Atmosphäre (IPA), Johannes Gutenberg-Universität, Mainz, Deutschland*

^g*Laboratoire de Météorologie Physique (LaMP), Université Clermont Auvergne, France*

^h*Institut für Meteorologie und Klimaforschung (IMK), Karlsruher Institut für Technologie (KIT),
Deutschland*

ⁱ*Abteilung für Partikelchemie, Max-Planck-Institut für Chemie (MPIC), Mainz, Deutschland*

^j*Physical Sciences Laboratory (PSL), National Oceanic and Atmospheric Administration
(NOAA), Boulder, Colorado, USA*

^k*Cooperative Institute for Research in Environmental Sciences (CIRES), University of Colorado,
Boulder, USA*

^l*Institut für Flugführung (IFF), Technische Universität Braunschweig, Deutschland*

^m*Institut für Mathematik, Universität Potsdam, Deutschland*

ⁿ*Abteilung für Umweltmeteorologie, Fakultät für Regionale und Umweltwissenschaften,
Universität Trier, Deutschland*

^o*Finnish Meteorological Institute (FMI), Helsinki, Finnland*

^p*Zentrum für Marine Umweltwissenschaften der Universität Bremen (MARUM), Deutschland*

^q*Deutsches Zentrum für Luft- und Raumfahrt (DLR), Oberpfaffenhofen, Deutschland*

^r*Centro de Estudos do Ambiente e do Mar (CESAM), Universidade de Aveiro, Portugal*

^s*Max-Planck-Institut für Meteorologie (MPIM), Hamburg, Deutschland*

^t*University of Warsaw (UW), Faculty of Physics, Warsaw, Poland*

^u*National Aeronautics and Space Administration (NASA), Goddard Space Flight Center,
Greenbelt, MD, USA*

^v*Shirshov Institute of Oceanology, Russian Academy of Sciences, Moscow, Russia*

^w*Now at: Laboratoire d'Optique Atmosphérique - CNRS, Université de Lille, France*

^x*Now at: Cooperative Institute for Research in Environmental Sciences (CIRES) and National
Snow and Ice Data Center (NSIDC), University of Colorado, Boulder, USA*

^y*Now at: Atmospheric Science, Department of Chemistry and Molecular Biology, University of
Gothenburg, Sweden*

^z*A. M. Obukhov Institute of Atmospheric Physics, Russian Academy of Sciences, Moscow, Russia*

Corresponding author: m.wendisch@uni-leipzig.de

ABSTRACT: Mechanisms behind the phenomenon of Arctic amplification are widely discussed. To contribute to this debate, the (\mathcal{AC})³ project has been established in 2016 (<http://www.ac3-tr.de/>). It comprises modeling and data analysis efforts as well as observational elements. The project has assembled a wealth of ground-based, airborne, ship-borne, and satellite data of physical, chemical, and meteorological properties of the Arctic atmosphere, cryosphere, and upper ocean that are available for the Arctic climate research community. Short-term changes and indications of long-term trends in Arctic climate parameters have been detected using existing and new data. For example, a distinct atmospheric moistening, an increase of regional storm activities, an amplified winter warming in the Svalbard and North Pole regions, and a decrease of sea ice thickness in the Fram Strait and of snow depth on sea ice have been identified. A positive trend of tropospheric bromine monoxide (BrO) column densities during polar spring was verified. Local marine/biogenic sources for cloud condensation nuclei and ice nucleating particles were found. Atmospheric/ocean and radiative transfer models were advanced by applying new parameterizations of surface albedo, cloud droplet activation, convective plumes and related processes over leads, and turbulent transfer coefficients for stable surface layers. Four modes of the surface radiative energy budget were explored and reproduced by simulations. To advance the future synthesis of the results, cross cutting activities are being developed aiming to answer key questions in four focus areas: lapse rate feedback, surface processes, Arctic mixed-phase clouds, and air mass transport and transformation.

CAPSULE: The German Transregional Collaborative Research Center (\mathcal{AC})³ investigates signs, causes and consequences of Arctic amplification by a unique combination of comprehensive observations, data analysis, and modeling across scales. First results achieved since 2016 are presented.

1. Introduction

In the last 20 to 30 years, a new Arctic has developed right before our eyes in response to global warming (Overland et al. 2011; Jeffries et al. 2013). Truly substantial and rapid changes of Arctic climate parameters have been observed; they continue to proceed at an unexpected speed and vehemence (Thoman et al. 2020; Moon et al. 2021). One prominent example of these ongoing climate changes is the dramatic decline of sea ice in the Arctic Ocean, which seems mainly be determined by atmospheric near-surface warming (Olonscheck et al. 2019). Overall, the Arctic sea-ice cover observed at the end of summer has halved in the past 40 years (Screen 2021). Another apparent sign of the current climate changes in the Arctic is the accelerated increase of the Arctic near-surface air temperature (SIDEBAR 1). Both and further obvious climate changes result from the elevated sensitivity of the Arctic climate system to global warming, compared to that at lower latitudes, which amplifies the impact of a variety of evolving local and remote processes and feedback mechanisms. The enhanced efficiency of these interlinked mechanisms is promoted by Arctic-specific characteristics (e.g., low sun, polar day and night, high surface albedo), and particular atmospheric circumstances (e.g., pronounced near-surface temperature inversions, frequent and persistent low-level clouds, widespread moisture inversions). Especially, mixed-phase clouds play a decisive role in feedback processes in the Arctic (Tan et al. 2021). The mechanisms behind the enhanced response of the Arctic climate system to global warming are generally referred to as Arctic amplification (Serreze and Francis 2006; Serreze and Barry 2011).

Knowledge on, and understanding of the processes and non-linear feedback mechanisms that determine Arctic amplification have been improving swiftly (Previdi et al. 2021). Still, the current ability to model the recent changes of the Arctic climate changes is limited and, therefore, the estimates of future evolution involve high uncertainties (Smith et al. 2019; Cohen et al. 2020). Important scientific gaps in understanding and quantifying the local and remote processes and feedbacks causing Arctic amplification still exist. These deficiencies particularly relate to the

representation of the key mechanisms in models (Block et al. 2020), the adequate description of the evolution of clouds (Pithan et al. 2014; Wendisch et al. 2019; Kretzschmar et al. 2020), the interactions of sea ice and ocean processes with the atmosphere (Rinke et al. 2019a) and clouds (Huang et al. 2019), and the understanding of processes determining air mass transformations during meridional transports of heat, moisture, and momentum by atmospheric circulation and ocean currents (Pithan et al. 2018; Nash et al. 2018; Wendisch et al. 2021). Additionally, the role of trace gases and aerosol particles in Arctic amplification is still uncertain (Schmale et al. 2021).

To resolve these issues, both long-term and campaign-based observations accompanied by detailed data analysis and dedicated numerical weather prediction and climate model simulations are required. These needs have motivated the establishment of the Transregional Collaborative Research Center (\mathcal{AC})³ (Wendisch et al. 2017) (<http://www.ac3-tr.de/>). The project aims to enhance the understanding of key local and remote atmospheric and surface processes and feedbacks driving Arctic amplification. This general objective is being achieved by a synergistic combination of observations using ground-based, airborne, ship-borne, and satellite-borne sensors, with comprehensive data analysis and modeling over a broad range of spatial and temporal scales. For this purpose, (\mathcal{AC})³ utilizes extensively the excellent Arctic research infrastructure made available by AWI¹ (Alfred-Wegener-Institut, Helmholtz-Zentrum für Polar- und Meeresforschung). Furthermore, the data collected during the MOSAiC (Multidisciplinary drifting Observatory for the Study of Arctic Climate) expedition (Shupe et al. 2022; Nicolaus et al. 2022; Rabe et al. 2022), to which (\mathcal{AC})³ provided a major German contribution, will help to reach the goals of (\mathcal{AC})³, in particular with regard to the annual cycle of local processes in the inner Arctic. Spectacular new data gathered during the recently completed HALO-(\mathcal{AC})³ airborne campaign (Wendisch et al. 2021) will contribute to clarify remote feedbacks of air mass transformations during warm air intrusions and cold air outbreaks.

The specific processes and feedback mechanisms that comprise the focus of (\mathcal{AC})³ are summarized in Section 2. Major results as well as prospects of the project are introduced by discussing three questions in the subsequent sections: What have we done so far (Section 3)? What did we learn (Section 4)? Where do we go from here (Section 5)? In the concluding Section 6 selected important results achieved within (\mathcal{AC})³ so far are summarized.

¹All acronyms are listed in Appendix A

SIDEBAR 1: Near-Surface Air Temperature – Changes Since 1960

The strong increase of the Arctic near-surface air temperature observed over the last decades represents one of the most evident signs of Arctic climate change. The first indications of an amplified warming in the Arctic, as compared to mid-latitude, tropical, and global warming, appeared in the mid-1990s (Fig. 1a). Since then, a gradually increasing divergence between Arctic and non-Arctic average near-surface air temperature has been observed. The strength of the amplified warming depends on the season with the largest warming in winter (Fig. 1b). The winter of 2017/18 showed the most dramatic indications of amplified warming in the Arctic observed so far, with a 2.8 K higher temperature compared to the global warming. During the last 30 years, the Arctic has warmed with respect to the proceeding 30-year period by 0.87 K to 1.63 K depending on season (Table 1a). This warming is much stronger than that observed in the mid-latitudes, the tropics, and globally. In addition, Table 1b quantifies the ratios of the averaged warming in the Arctic with respect to the mid-latitudes, the tropics, and the global warming, which can be interpreted as Arctic amplification factors. They range between 1.32 and 2.96, depending on the reference region and season with largest values in winter and spring.

TABLE 1: (a) Averaged (1991–2021) increase of the Arctic near-surface air temperature as compared to the reference period of 1951–1980. (b) Arctic amplification factors (ratio of averaged warming in the Arctic in relation to mid-latitudes, tropics, and the globe). The same data source as in Fig. 1 has been used.

(a) Averaged Warming (K)					
	Annual	DJF	MAM	JJA	SON
Arctic	1.33	1.49	1.63	0.87	1.33
Mid-Latitudes	0.71	0.77	0.75	0.66	0.64
Tropics	0.54	0.51	0.55	0.55	0.54
Global	0.60	0.60	0.62	0.58	0.58
(b) Arctic Amplification Factors					
	Annual	DJF	MAM	JJA	SON
Arctic/Mid-Latitudes	1.87	1.94	2.17	1.32	2.08
Arctic/Tropics	2.46	2.92	2.96	1.58	2.46
Arctic/Globe	2.22	2.48	2.63	1.50	2.29

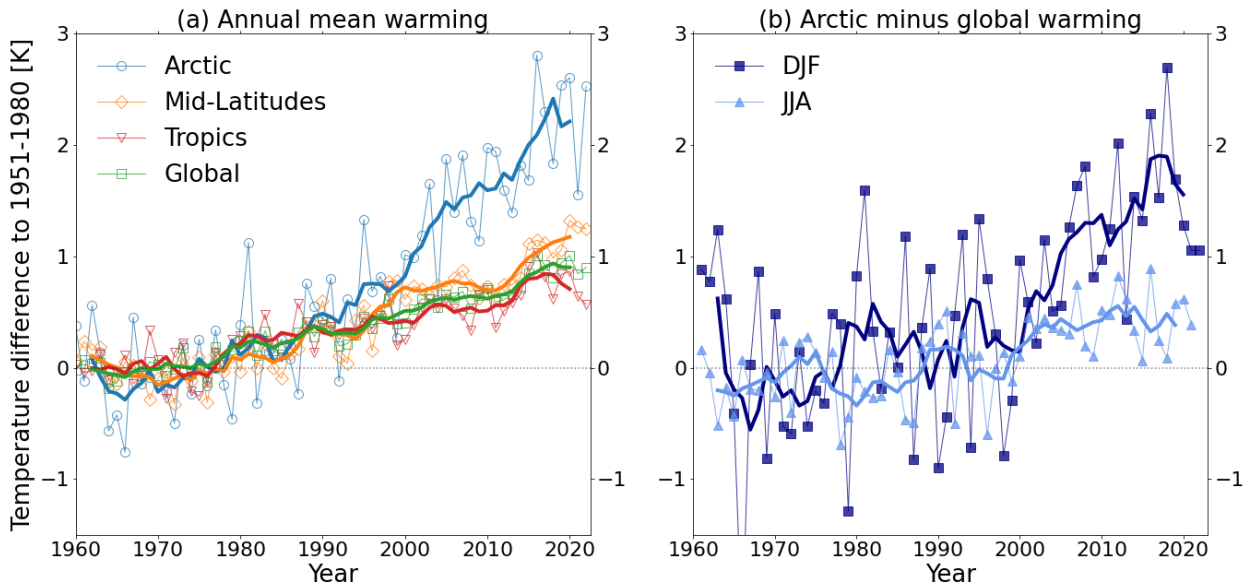


FIG. 1: Time series of zonally and meridionally averaged, near-surface air temperature differences (anomalies). (a) shows the annually averaged differences of the near-surface air temperature relative to the corresponding long-term mean over the time period of 1951-1980 for the Arctic (60° – 90° N), Mid-Latitudes (30° – 60° N), Tropics (20° S – 20° N), and the globe. (b) illustrates the difference of the warming in the Arctic shown in (a), and the global average warming for winter (DJF) and summer (JJA). The thick lines in (a) and (b) without symbols indicate five-year running averages. The curves for spring (MAM) and fall (SON) are similar to those for DJF, and therefore have been omitted in (b). The data are provided by the NASA GISTEMP Team, 2020: GISS Surface Temperature Analysis (GISTEMP), version 4. NASA Goddard Institute for Space Studies. Data set accessed at <https://data.giss.nasa.gov/gistemp/> on 8 June 2022.

2. The $(\mathcal{AC})^3$ Framework of Processes Determining Arctic Amplification

Arctic amplification involves a number of intertwined chains of effects, some of which are shown in Fig. 2, which provides the major framework for the investigations carried out within $(\mathcal{AC})^3$. The figure illustrates important and interlinked local and remote atmospheric and surface processes and feedback mechanisms that contribute to Arctic amplification. They include largely atmospheric and marine effects related to the Arctic atmosphere, upper ocean, and sea ice. The role of the land surfaces in Arctic amplification is not a focus of $(\mathcal{AC})^3$. In the following Subsections a–d, the processes and feedbacks in Fig. 2 are introduced.

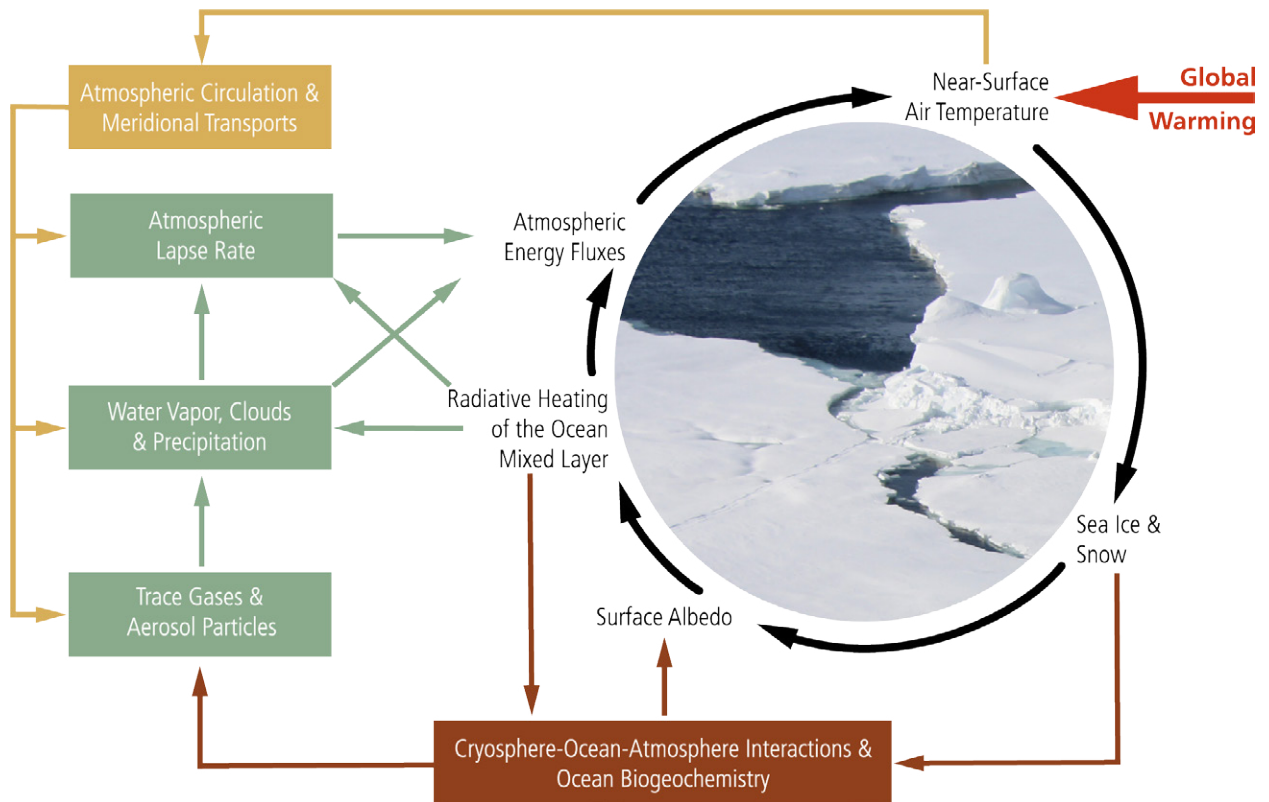


FIG. 2: The (\mathcal{A})³ simplified schematic of important local and remote processes and feedback mechanisms driving Arctic amplification. The figure illustrates the initial trigger by *Global Warming* (red), and shows examples of processes/feedback mechanisms such as: *a. Surface Albedo Feedback* (black), *b. Upper Ocean Effects* (brown), *c. Local Atmospheric Processes* (green), and *d. Arctic – Mid-latitude Linkages* (yellow). Adopted from Wendisch et al. (2017) in modified form.

a. Surface Albedo Feedback: Positive (Black in Fig. 2)

Triggered by *global warming*², the *near-surface air temperature* in the Arctic increases. As a result, *sea ice & snow* melt and the *surface albedo* of the Arctic Ocean decreases. Therefore, more solar radiation is absorbed by the increasingly darker open (sea ice-free) ocean surface, leading to a *radiative heating of the ocean mixed layer*. This enhances the radiative (solar and terrestrial) and turbulent (heat, moisture) *atmospheric energy fluxes*. For example, the upward terrestrial radiative energy flux densities (irradiances) emitted by the warmer ocean surface are absorbed by near-surface atmospheric greenhouse gases (e.g., water vapor) and/or clouds and then re-emitted

²Terms from Fig. 2 are highlighted in the text of Section 2 in italic style

towards the surface. This in turn further increases the *near-surface air temperature* establishing a positive feedback loop.

This amplifying feedback mechanism is well known as the direct surface albedo feedback (Arrhenius 1896; Budyko 1969; Sellers 1969; Manabe and Wetherald 1975). It is most effective in summer when sufficient solar radiation reaches the surface of the Arctic Ocean. Apart from that, the surface albedo feedback works also indirectly and delayed. The solar radiative energy absorbed in the open ocean mixed layer during spring and summer is converted into heat that is stored in the upper ocean. The saved heat energy determines the onset of re-freezing in fall. Prior to the re-freezing in late fall and early winter, the stored heat is released into the atmosphere via radiative and turbulent processes, warming the near-surface air, and thus causing a delayed, indirect warming effect. After the onset of re-freezing, the increasing sea ice cover reduces the energy exchange between the ocean mixed layer and near-surface air due to thermal insulation.

There is general consensus that the direct surface albedo feedback represents one of the important causes for Arctic amplification in spring (Hall 2004; Screen and Simmonds 2010; Taylor et al. 2013). The indirect surface albedo feedback contributes to Arctic amplification in fall and winter (Pithan and Mauritsen 2014; Goosse et al. 2018).

b. Upper Ocean Effects – Positive or Negative (Brown in Fig. 2)

The expanding open ocean areas, resulting from the enhanced melting of *sea ice & snow* in a warmer Arctic, cause intensified *cryosphere-ocean-atmosphere interactions* and, as a consequence, increased emissions of *trace gases & aerosol particles* of marine/biogenic origin. Furthermore, *ocean biogeochemistry* processes in the upper ocean mixed layer are amplified (Ardyna and Arrigo 2020), in particular the primary productivity³. This may cause an enhanced *radiative heating of the ocean mixed layer* by increased absorption of solar radiation. This heating in turn raises the temperature of the ocean mixed layer, further amplifying cryosphere-ocean-atmosphere interactions and ocean biogeochemistry processes. Additionally, the upper ocean will become less stable in terms of the halocline (Polyakov et al. 2017). Altogether, the role of the oceanic heat transport in warming the lower atmosphere is promoted (Tsubouchi et al. 2021).

³Primary productivity considers the rate at which energy is converted to organic substances by photosynthesis.

c. *Local Atmospheric Processes: Positive or Negative (Green in Fig. 2)*

The enhanced emissions of *trace gases* discussed above influence the magnitude of the Arctic amplification (Greenhouse effect) and the oxidation capacity of the atmosphere. Arctic *aerosol particles*, including CCN (Cloud Condensation Nuclei) and INPs (Ice Nucleating Particles), are released over the ice-free ocean by wind drag (wind-wave driven), *ocean biogeochemistry* processes, new particle formation from the release of iodine, or biological activities.

Due to the *radiative heating of the ocean mixed layer*, the ocean surface warms up, causing an increase of *water vapor* concentration due to intensified evaporation. This enhances the downward terrestrial radiative *atmospheric energy fluxes*, thus further increasing the *near-surface air temperature*. Furthermore, the higher *water vapor* amounts advance the formation of low-level *clouds*, which also increase the emission of downward terrestrial irradiances. During polar night this leads to a general warming of the near-surface air (positive feedback), while in summer the solar cloud cooling effect may outweigh the terrestrial warming (negative feedback). However, due to the bright surfaces and low solar zenith angles, the net effect of clouds in the central Arctic is mostly a surface warming (Shupe and Intrieri 2004). Thus, in a warming Arctic with possibly more clouds, an initial warming is mostly amplified over sea ice (positive feedback). However, as sea ice retreats and darker open ocean surfaces are exposed, the cooling effect by clouds could play a bigger role in summer. On the other hand, no cloud response to sea ice loss has been detected during summer between 2006-2008, a period with low summer sea ice concentrations (Kay and Gettelman 2009). Instead, such a cloud response was detected in fall. Therefore, Kay and Gettelman (2009) conclude that cloud changes resulting from sea ice loss play a minor role during summer, but may contribute to a cloud-ice feedback during early fall.

The future evolution of cloud properties will have an impact on *precipitation*. While total precipitation in the Arctic is predicted to increase in the future, snowfall in winter is projected to stay roughly constant and to decrease in summer and fall (McCrystall et al. 2021).

The *atmospheric lapse rate* feedback comprises an important atmospheric process with respect to Arctic amplification (Block et al. 2020; Lauer et al. 2020; Boeke et al. 2021; Linke and Quaas 2022). In the Arctic, vertical atmospheric turbulent transport is commonly inhibited by a very stable and shallow ABL (Atmospheric Boundary Layer). Consequently, the warming of the near-surface air due to *radiative heating of the ocean mixed layer* is mostly kept to the ABL. The

resulting enhanced downward terrestrial radiative *atmospheric energy fluxes* further increase the *near-surface air temperature*. However, the increased surface temperature also initiates convection weakening the warming effect of the lapse rate feedback. At the top of the atmosphere, the diminished increase in outgoing terrestrial radiative energy, compared to a vertically homogeneous temperature change, is relevant and implies the overall relative warming effect.

d. Arctic – Mid-latitude Linkages: Positive or Negative (Yellow in Fig. 2)

Atmospheric circulation & meridional transports are suspected to change due to the decreasing meridional geopotential gradient caused by the enhanced warming of the Arctic compared to mid-latitudes (Francis and Vavrus 2015). This effect likely causes a slower west wind drift and larger Rossby wave amplitudes moving with a slower phase speed, although other teleconnections or even internal variability may also be a reason for the increased waviness (Blackport and Screen 2020). The enhanced amplitudes and stationarity of the Rossby waves would promote the meridional transport of trace gases, aerosol particles, heat, water vapor, clouds, and precipitation into and out of the Arctic by means of more frequent warm/moist air intrusions and cold/dry air outbreaks. During the meridional transport, remote feedback mechanisms involving the vertical thermodynamic structure (*atmospheric lapse rate*) of the transported air masses, as well as combined effects including *water vapor, clouds & precipitation* as well as *aerosol particles* link Arctic and mid-latitude processes in a complex manner (Wendisch et al. 2021). There seems to be growing evidence that such links actually exist, for example with regard to sea ice loss (Screen 2021; Crawford et al. 2022). However, the current generation of models struggles to represent the modification of regional and large-scale atmospheric circulation and of air mass properties along meridional transports likely caused by enhanced warming of the near-surface air temperature in the Arctic (Cohen et al. 2014; Francis and Vavrus 2015; Pithan et al. 2018; Armour et al. 2019; Cohen et al. 2020).

3. What have we done so far?

The focus in Sections 3 and 4 is to document and summarize some of the specific contributions from (\mathcal{AC})³ to the international research on Arctic amplification. Whereas the current Section 3 introduces observational activities, retrieval developments, corresponding data analysis,

and modeling applications, Section 4 will elaborate the scientific results of $(\mathcal{AC})^3$. Of course, the work conducted in $(\mathcal{AC})^3$ builds upon a rich history of Arctic research. Therefore, we have tried to concisely put the findings of $(\mathcal{AC})^3$ into context with the existing literature. For a more detailed discussion of the progress achieved in $(\mathcal{AC})^3$, the reader is encouraged to consult the specific $(\mathcal{AC})^3$ publications, compiled at <https://publons.com/researcher/3796220/ac3-arctic-amplification/>.

a. Ground-based, Airborne, and Ship-borne Measurements

An important pillar of $(\mathcal{AC})^3$ is the collection of comprehensive data sets as a basis for the study of Arctic amplification. The Fram Strait area northwest of Svalbard and Northern Greenland, as one of the most sensitive regions for the Arctic climate system, became a hot spot of ground-based, airborne, and ship-borne activities during $(\mathcal{AC})^3$. Successful measurements in this area have provided an immense treasure of data, covering a broad range of spatial and temporal scales, different seasons, as well as meteorological and sea ice conditions.

Ground-based and vertically resolved data were obtained during continuous observations at the permanent joint German–French AWIPEV (Alfred Wegener Institute for Polar and Marine Research and the French Polar Institute Paul Emile Victor) research base in Ny-Ålesund (Spitsbergen, Fig. 3). Measurements at Ny-Ålesund have shown that clouds occurred around 80 % of the time, mostly below 2 km altitude (Fig. 3d) (Nomokonova et al. 2019). Most of the time clouds contained ice; the relative occurrence of liquid water and ice clouds was mainly influenced by the prevailing synoptic conditions, e.g., wind direction, and thermodynamic coupling with the surface (Gierens et al. 2020). Multi-layer clouds (45 %) and single-layer mixed-phase clouds (20 %) were dominant. During $(\mathcal{AC})^3$ the instrumentation of the AWIPEV research base was extended and new retrieval algorithms were developed to enable sophisticated cloud and precipitation measurements (Nomokonova et al. 2019). Furthermore, instruments to detect the seasonal variability and secular trends of several long and short lived trace gases through the global measurement networks NDACC (Network for the Detection of Atmospheric Composition Change) and TCCON (Total Carbon Column Observing Network) with enhanced observation frequency were operated at AWIPEV (Buschmann et al. 2017). In addition, the tethered balloon BELUGA (Balloon-borne modular Utility for profilinG the lower Atmosphere) (Egerer et al. 2019) and the unmanned

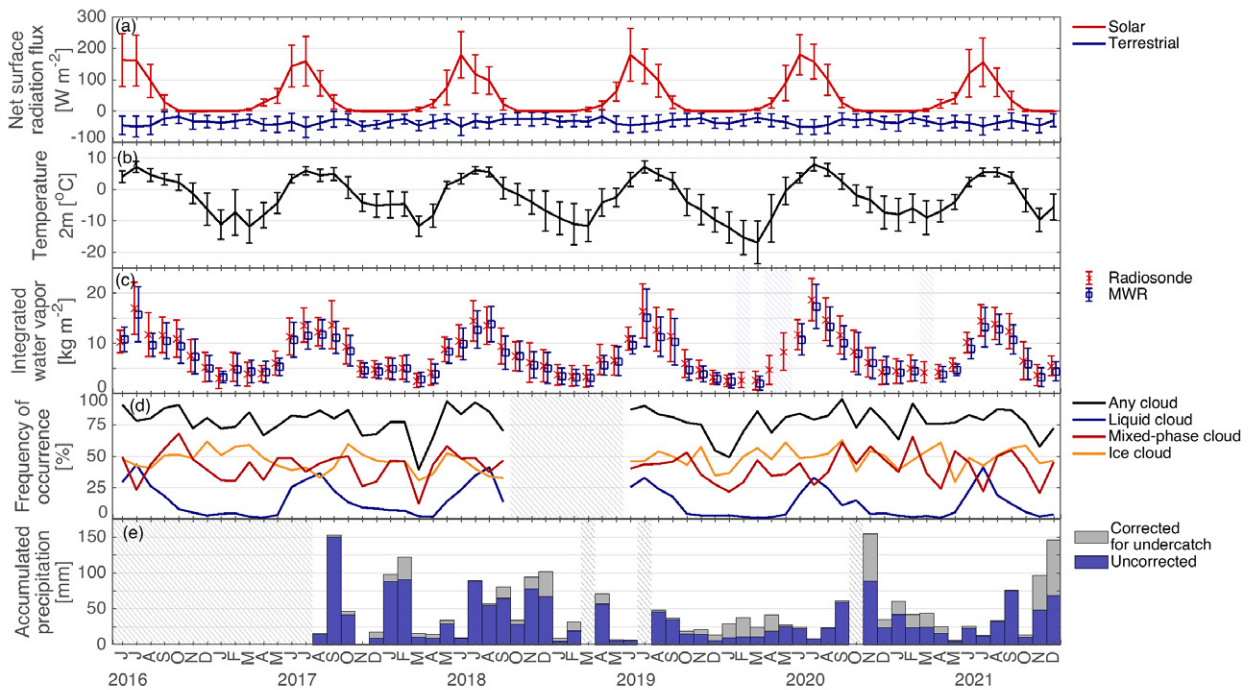


FIG. 3: Time series of selected atmospheric observations collected at the AWIPEV research base at Ny-Ålesund during $(AC)^3$. (a) Monthly mean solar (red) and terrestrial (blue) net (downward minus upward) surface irradiance, (b) monthly mean 2 m-temperature, (c) monthly mean vertically integrated water vapor from microwave radiometer (MWR; blue) and radiosondes (red), (d) monthly frequency of occurrence of any type of clouds (black), liquid clouds (blue), mixed-phase clouds (red) and ice clouds (orange) in the atmospheric column based on a cloud radar and ceilometer synergy, (e) monthly accumulated precipitation from Pluvio weighing gauge based on original (blue) and corrected values (grey). The error bars in (a) and (c) represent the standard deviation of the daily mean values. Hatched areas indicate times where no or insufficient data are available to calculate monthly mean values.

aerial system ALADINA (Application of Light-weight Aircraft for Detecting in-situ Aerosols) (Lampert et al. 2020) were launched during dedicated intensive operational phases covering small scales up to 1.5 km altitude with high-resolution meteorological, turbulence, aerosol, and radiation measurements.

Four airborne campaigns were performed using the German research aircraft Polar 5 and Polar 6 of AWI (Wesche et al. 2016): ACLOUD (Arctic CLOUD Observations Using airborne measurements during polar Day) in May/June 2017 (Wendisch et al. 2019), PAMARCMiP (Polar Airborne Measurements and Arctic Regional Climate Model Simulation Project) in March/April 2018,

AFLUX (Airborne measurements of radiative and turbulent FLUXes in the cloudy atmospheric boundary layer) in March/April 2019, and MOSAiC-ACA (Atmospheric Airborne observations in the Central Arctic) in August/September 2020. The aircraft observations provided a rich data set covering the northwestern segment of Svalbard and the area north of Villum Research Station (Fig. 4a) over an altitude range of up to 4 km (Fig. 4b). The two aircraft were extensively equipped with partly newly developed instruments (Ehrlich et al. 2019; Mech et al. 2022), such as the new airborne MiRAC (Microwave Radar/radiometer for Arctic Clouds) (Mech et al. 2019).

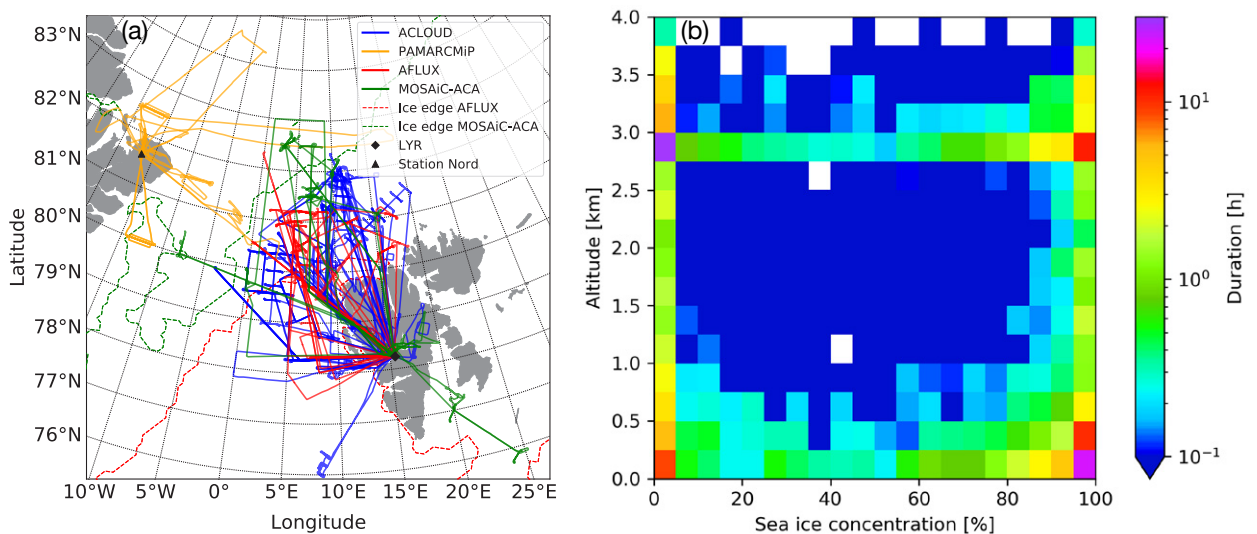


FIG. 4: Horizontal and vertical coverage of the aircraft observations conducted during ACLOUD (82+82 flight hours with Polar 5 and Polar 6), PAMARCMiP (40 flight hours, Polar 5), AFLUX (66 flight hours, Polar 5), and MOSAiC-ACA (44 flight hours, Polar 5) altogether 314 hours of measurements (about 10 % within clouds) were collected. (a) Horizontal projections of flight pattern during the airborne measurements, LYR refers to Longyearbyen on Svalbard, (b) Vertical distribution of number of flight hours spent in different altitudes over different sea ice conditions.

The ship-borne research cruise PASCAL (Physical feedback of Arctic ABL, Sea ice, Cloud and Aerosol) using the RV (Research Vessel) Polarstern of AWI was conducted in May/June 2017 (Wendisch et al. 2019). PSACAL was closely coordinated with ACLOUD, most of the flight hours of the two polar aircraft were spent sampling the vertical column above RV Polarstern, which comprises a unique observational approach. Furthermore, $(\mathcal{AC})^3$ has significantly contributed to the MOSAiC expedition with RV Polarstern performed between September 2019 and October 2020 (Shupe et al. 2022; Nicolaus et al. 2022; Rabe et al. 2022). The tethered balloon system BELUGA was deployed during both PASCAL (Egerer et al. 2021) and MOSAiC (Lonardi et al. 2022).

Furthermore, the helicopter-borne instrument sonde HELiPOD was flown during MOSAiC (Shupe et al. 2022). Also, the OCEANET-Atmosphere facility, extended by the motion-stabilized cloud radar Mira-35 (Griesche et al. 2020) and the passive part of MiRAC, was operated continuously during PASCAL and MOSAiC (Engelmann et al. 2021; Walbröl et al. 2022). The ship-based observations conducted during PASCAL revealed a high fraction of low-level stratus clouds in summer (Griesche et al. 2020). These clouds below an altitude of 150 m were observed 25 % of the time.

b. Satellite Data Analysis

Important work on developing new satellite retrieval algorithms and combining data from different sensors to retrieve aerosol particle, cloud, and surface properties was performed within $(\mathcal{AC})^3$. A summary of the satellite data employed during $(\mathcal{AC})^3$ is given in the SUPPLEMENTARY MATERIALS (Table 1). Here we can just introduce some of the $(\mathcal{AC})^3$ activities in this area. Mei et al. (2018) developed a novel algorithm for the derivation of COT (Cloud Optical Thickness) and CER (Cloud Effective Radius) for ice clouds from satellite data with promising results over snow and sea ice. Jafariserajehlou et al. (2019) developed a new cloud masking technique specialized for the Arctic, which can be used for long-term aerosol retrievals over sea ice, and whose quality depends heavily on the quality of the cloud mask. Mei et al. (2020a) proposed a unique retrieval technique to retrieve the coarse mode fraction of aerosol particles above snow and ice. Furthermore, Mei et al. (2021a) have developed and globally validated a new retrieval of snow properties based on a thorough sensitivity study (Mei et al. 2021b). Innovative retrieval techniques to derive the Integrated Water Vapor (IWV) have been introduced merging observations from different microwave satellite sensors (Triana-Gómez et al. 2018, 2020). The first consistent and consolidated long-term (1996-2017) data set of bromine monoxide (BrO) over the Arctic region has been derived from four different ultraviolet–visible satellite instruments (Bougoudis et al. 2020). In addition, a new high-resolution retrieval algorithm for column densities of BrO has been developed (Seo et al. 2019). Long-term (2002-today) time series of phytoplankton groups were derived (Losa et al. 2017; Xi et al. 2021), which for the first time also deliver phytoplankton group data sets for the Arctic Ocean.

Several snow and sea ice parameters have been retrieved using microwave observations (Scarlat et al. 2017, 2020). The accuracy of sea ice concentration measurements has been improved (Lu et al. 2018, 2022), as well as their spatial resolution, by combining infrared and microwave data (Ludwig et al. 2020). Also, the retrieval accuracy of the thickness of thin sea ice was increased (Pařilea et al. 2019). Work conducted within $(\mathcal{AC})^3$ delivered the first data set of snow depth on sea ice for the complete Arctic including multi-year sea ice (MYI) regions in spring and first-year sea ice (FYI) from October to May (Rostosky et al. 2018, 2020). By including lower microwave radiometer frequencies at 7 GHz, a more reliable retrieval and an extension to MYI could be achieved, which was not possible with previous methods (Markus et al. 2006). The uncertainty of retrievals of snow depth on sea ice was calculated based on a Monte-Carlo simulations (Rostosky et al. 2020), it increases with increasing snow depth and is higher over MYI than over FYI. Roughly, the relative uncertainty is about 20-30 % of the snow depth. Figure 5 shows an example of the sea ice data sets retrieved within $(\mathcal{AC})^3$.

c. Atmospheric/Ocean and Radiative Transfer Models

Newly developed and further refined numerical models covering a broad range of temporal and spatial scales were applied within $(\mathcal{AC})^3$, a summary can be found in Table 2 of the SUPPLEMENTARY MATERIALS. A Lagrangian LES (Large-Eddy Simulations) setup was developed for the Arctic to follow trajectories of an air mass at high latitudes (Neggers et al. 2019). A specific LES version of the atmospheric ICON (ICOsahedral Non-hydrostatic) model with realistic forcing and considering a heterogeneous surface was applied representing the complex environment of Ny-Ålesund (Schemann and Ebell 2020). By combining the model output with the instrument simulator PAMTRA (Passive and Active Microwave radiative TRAnsfer tool for simulating radiometer and radar measurements of the cloudy atmosphere) (Mech et al. 2020), the detection of mixed-phase clouds by specific instruments was modeled with unprecedented resolution down to 75 m (Fig. 6). ICON was operated in a nested mode for an Arctic domain with a horizontal resolution of down to 2 km, to improve the representation of Arctic clouds (Kretzschmar et al. 2020) and intense moisture intrusion events (Bresson et al. 2022). For larger scales (9-25 km), the coupled ocean-atmosphere HIRHAM (High-Resolution Limited Area Model)-NAOSIM (North Atlantic/Arctic Ocean-Sea Ice Model) regional model system was established (Dorn et al. 2019; Rinke et al. 2019a). Output from

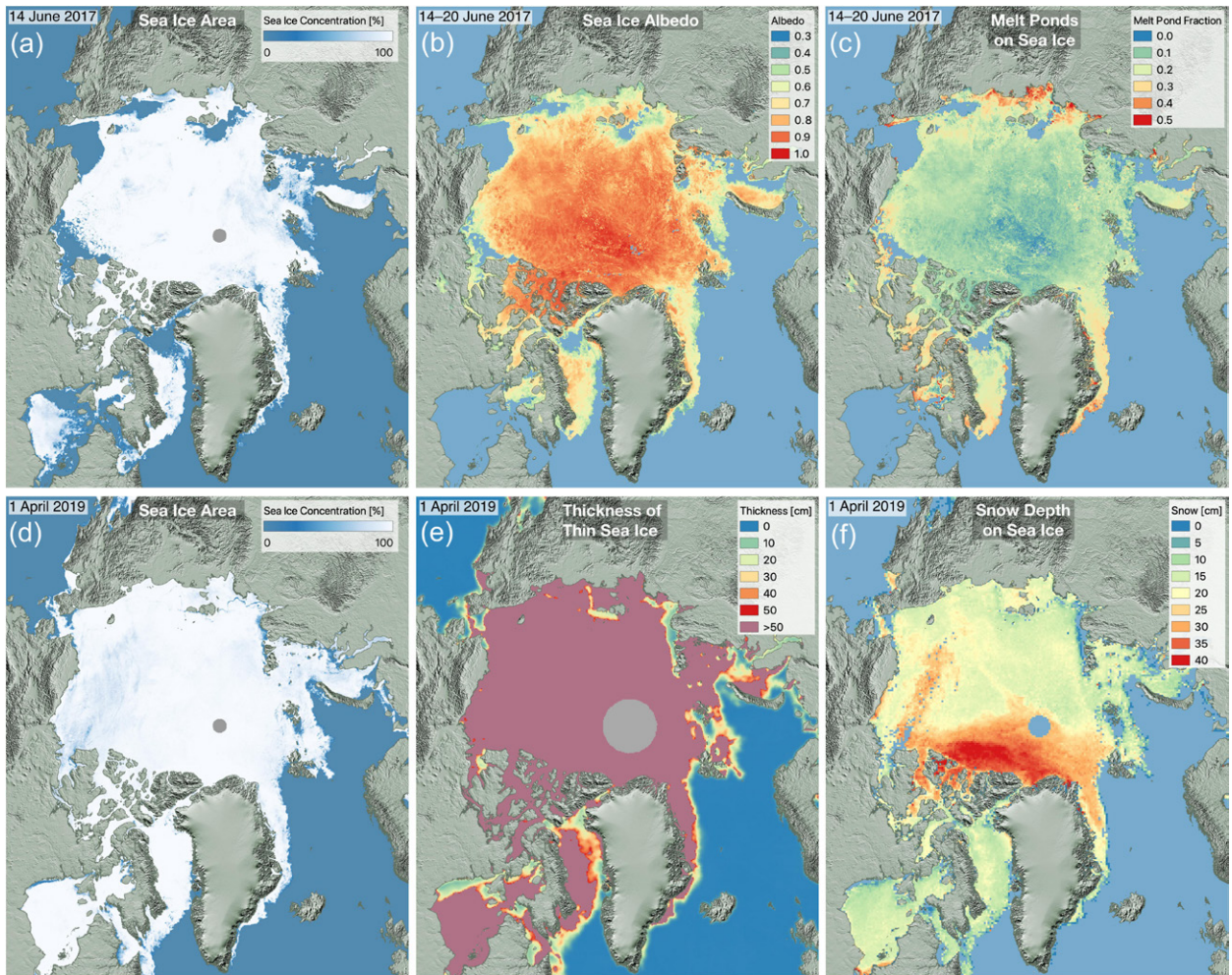


FIG. 5: Sea ice conditions from satellite observations during the ACLOUD (a-c) and AFLUX (d-f) campaigns. (a), (d) Sea ice concentration from the AMSR2 microwave radiometer. (b), (c) Sea ice albedo and fractional coverage of melt ponds on the sea ice from Sentinel-3 data (Pohl et al. 2020). (e) Thickness of thin sea ice from combined SMAP and SMOS L-band radiometer observations (Pařilea et al. 2019). (f) Snow depth on sea ice from AMSR2 observations (Rostosky et al. 2018, 2020). All data are available from <https://seaice.uni-bremen.de>.

the sixth-generation atmospheric general circulation model ECHAM6 and CMIP5 (Coupled Model Intercomparison Project Phase 5) global multi-model ensemble simulations has been analyzed to improve cloud representation (Kretzschmar et al. 2019) and radiative feedback understanding (Block et al. 2020). The fast ozone module SWIFT (Fast ozone chemistry scheme for interactive calculation of the extrapolar stratospheric ozone layer in coupled general circulation models) (Wohltmann et al. 2017), which efficiently calculates stratospheric ozone chemistry and enables

mutual ozone-climate interactions in GCMs (global circulation models), has been implemented into ECHAM6 (Romanowsky et al. 2019).

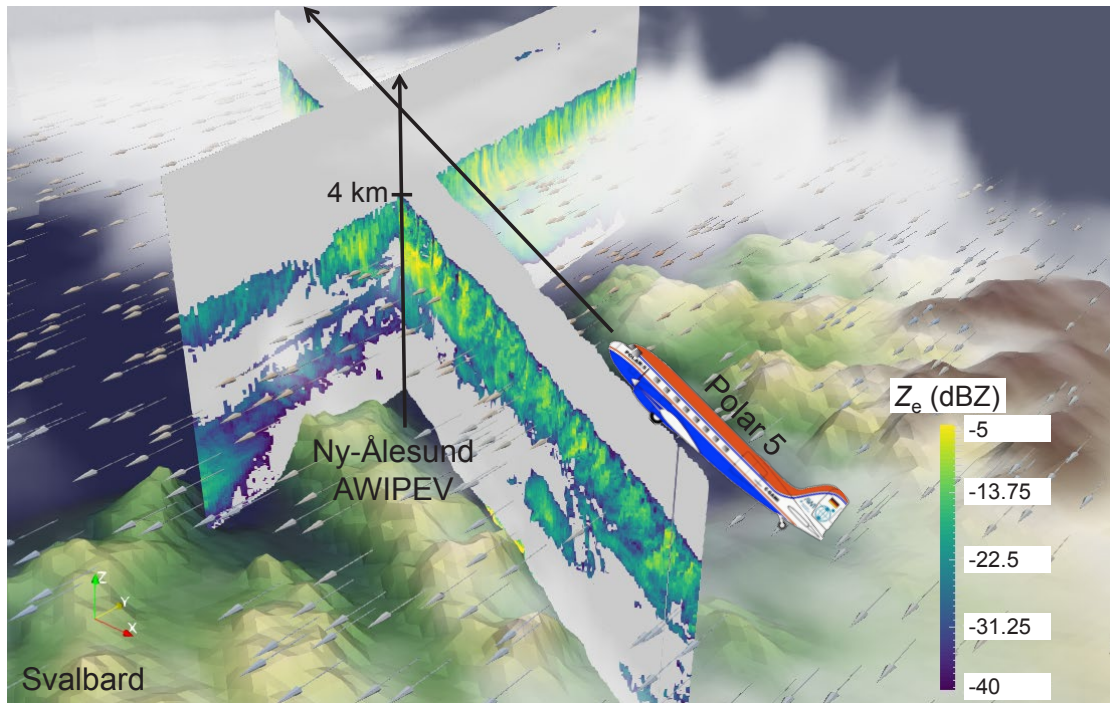


FIG. 6: Radar reflectivity Z_e (in dBZ) observations of airborne (curtain from lower right to upper left corners, measured by the flying downward pointing 94 GHz MiRAC radar installed on Polar 5) and ground-based (curtain from lower left to upper right corners, measured by the locally fixed upward pointing 94 GHz radar operated at the AWIPEV research base at Ny-Ålesund, whereby the vertically resolved column measurements were shifted with the simulated wind, indicated by the arrows) remote sensing measurements combined with high-resolution simulations (ICON-LEM, wind arrows, rendered clouds) around the area of Svalbard (topography).

Several radiative transfer models of different complexity have been improved within (\mathcal{AC})³ to investigate Arctic-specific radiative effects. For example, the coupled ocean-atmosphere radiative transfer model SCIATRAN (Radiative Transfer and Retrieval Algorithm) (Rozanov et al. 2017), and the coupled sea ice-ocean-biogeochemical model MITgcm (Massachusetts Institute of Technology General Circulation Model, <http://mitgcm.org/>) were extended to assess the feedback of surface ocean biogeochemistry on Arctic amplification (Soppa et al. 2019; Pefanis et al. 2020). New aerosol types specifically considering Arctic conditions were incorporated into SCIATRAN (Mei et al. 2020b). In addition, several ice crystal databases (Baum et al. 2011; Yang et al. 2013) have been included, allowing optimized radiative transfer simulations for Arctic ice and mixed-

phase clouds. Furthermore, new modules for the bidirectional reflectance distribution function (BRDF) of snow, white ice, and melt ponds have been implemented into SCIATRAN (Mei et al. 2022). The fast and accurate radiative transfer model FASMAR (Fast and Accurate Semi-analytical Model of Atmosphere-surface Reflectance) was newly developed to specifically consider for large solar zenith angles (larger than 80°), common in the Arctic, while other existing models are typically either limited to solar zenith angle smaller than 70° , or are too slow to process long-term datasets (Mei et al. 2020a). Furthermore, the one-dimensional libRadtran and RRTMG (Rapid Radiative Transfer Model for GCMs) software packages for radiative transfer were used to estimate the radiative forcing of Arctic clouds (Ebell et al. 2020; Barrientos-Velasco et al. 2022; Stapf et al. 2020, 2021; Stapf 2021). In addition, the new and computationally highly efficient, three-dimensional, backward Monte Carlo radiative transfer code LEIPSIC (Light Estimator Including Polarization, Surface Inhomogeneities, and Clouds) was developed and applied to quantify the impact of multiple scattering between clouds and a heterogeneous sea ice/ocean surface on satellite observations and the radiative energy budget in Arctic-specific conditions (Sun et al. 2020).

4. What did we learn?

a. Surface Albedo Feedback (Black in Fig. 2)

Here we provide examples of selected results with regard to the main components of the surface albedo feedback: *a-1. Sea Ice & Snow*, *a-2. Surface Albedo*, *a-3. Radiative Heating of the Ocean Mixed Layer*, and *a-4. Atmospheric Energy Fluxes*.

a-1. Sea Ice & Snow: Temporal Trends and Conditions During MOSAiC

We begin with some results of $(\mathcal{AC})^3$ with regard to sea ice and snow, which represent crucial components for the surface albedo effect. Temporal changes of these variables have been observed using partly newly developed methods. For example, combined satellite and ocean mooring data have shown that the mean sea ice thickness in the Fram Strait decreased by 15 % per decade during 1990–2014 (Spreen et al. 2020). Primarily due to this thinning, the Arctic sea ice volume export decreased by 27 % per decade between 1992 and 2014. Previous estimates from models and observations (Spreen et al. 2009; Zhang et al. 2017) did not find a significant decrease of the

ice volume export. These former estimates ended in earlier years, when the ice thinning was not as dominant.

With regard to snow depth on sea ice, it was found that in March 2015, the average snow depth on MYI was 31 cm, which is about twice the snow depth determined for FYI of 16 cm (Fig. 7a). Furthermore, a significant decrease of snow depth on sea ice of 2 cm per decade for FYI, and 3 cm per decade for MYI was identified in the March time series of 2003-2020 (Fig. 7b). The snow depth trends vary regionally with strongest values in the Atlantic Sector and the Kara and Laptev Seas, while other regions did not show significant trends. The inter-annual variability of the snow depth on MYI appeared much higher than on FYI, which showed a pronounced decline between 2009 and 2014 (Figs. 7c and 7d).

Also it was found that during the MOSAiC expedition, sea ice was thinner than in previous years and the drift of the MOSAiC ice flow was about 25 % faster than expected from climatology (Krumpen et al. 2021). However, the sea ice concentration, snow, and lead fraction were close to the climatological average.

a-2. Surface Albedo: Parameterization for Models

To improve the model representation of the surface albedo feedback, HIRHAM-NAOSIM has been upgraded with an adjusted sea ice albedo parameterization derived from field measurements during ($\mathcal{A}C$)³ (Jäkel et al. 2019). The former version has shown significant differences of the parameterized sea ice albedo compared to observations. Therefore, the sea ice albedo parameterization was adjusted with respect to changes in temperature-dependent snow properties and threshold temperatures describing the transition between dry and melting snow/ice. Further, the dependence of surface albedo on cloud occurrence was implemented, since the broadband albedo of snow and sea ice increased significantly compared to cloud-free conditions (Stapf et al. 2021). As a result, the root-mean-squared deviation between parameterized and measured surface albedo could be reduced from 0.14 to 0.04 for cloud free and broken cloud situations. The revised surface albedo parameterization has led to a more realistic magnitude of the overall sea ice loss from May to August as simulated by HIRHAM-NAOSIM. Also for ICON, the consideration of surface albedo measurements in nested high-resolution model runs improved the representation of the Arctic surface radiative energy budget significantly (Wendisch et al. 2019).

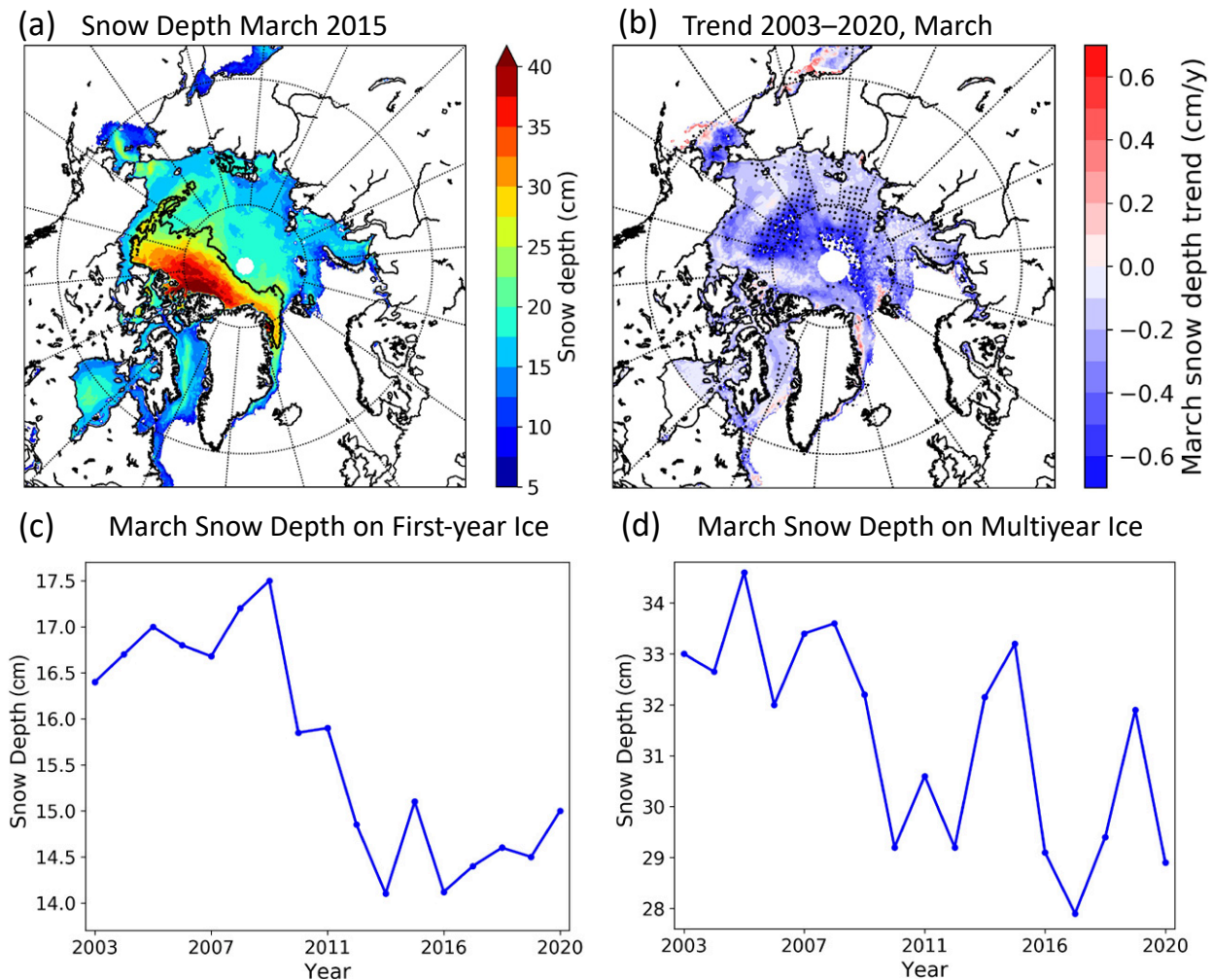


FIG. 7: (a) Average March 2015 snow depth on sea ice from AMSR2 satellite microwave radiometer observations. The black line discriminates first-year from multi-year sea ice. (b) Trend of March snow depth for years 2003 to 2020. Areas with dotted shading mark statistically significant trends. (c) Time series of yearly March snow depth on first-year sea ice (FYI) and (d) on multi-year sea ice (MYI). See Rostosky et al. (2018, 2020).

a-3. Radiative Heating of the Ocean Mixed Layer: A Self-Reinforcing Positive Feedback Loop

Biological particles embedded in the upper ocean water, such as PG (Phytoplankton Groups), CDOM (Colored Dissolved Organic Matter), and TSM (Total Suspended Matter), absorb solar radiation, which heats the upper part of the ocean mixed layer. If biological activity increases with rising ocean temperatures, the heating may reinforce itself in a positive feedback loop, thus contributing to reducing the sea ice cover even further. To investigate the importance of this effect in the Arctic Ocean, satellite ocean color observations were analyzed within $(\mathcal{AC})^3$. Respective

new satellite data products were developed for PG (Losa et al. 2017), CDOM, and TSM (Soppa et al. 2019). The resulting time series revealed changes of PG in the Fram Strait significantly affecting surface albedo (Losa et al. 2017). Correspondingly, SCIATRAN and MITgcm were applied to quantify the influence of CDOM and TSM on the radiative heating of the Laptev Sea shelf waters (Soppa et al. 2019) and the Arctic Ocean (Pefanis et al. 2020). It was shown that in Arctic summer, due to high levels of CDOM, 43 % more solar radiative energy is absorbed in the near-surface ocean water compared to situations with low CDOM, leading to radiative heating of the upper ocean water of 0.6 K per day. Thus, the expected future increase of CDOM and TSM discharge into the Laptev Sea, due to permafrost thawing, will likely accelerate the melting of sea ice and lead to enhanced ocean-atmosphere heat fluxes. To upscale this assessment, numerical experiments were conducted with and without incorporating the effect of PG and CDOM on solar absorption (Pefanis et al. 2020). These simulations indicated higher surface temperatures and more sea ice melt in summer. As a consequence, the sea ice season over parts of the Siberian shelf shortens by up to one month.

a-4. Atmospheric Energy Fluxes: Turbulence Parameterization and Impact of Leads

Common parameterizations tend to overestimate the turbulent energy fluxes for the often stably stratified Arctic surface layers. This issue has been overcome within $(\mathcal{AC})^3$ by Gryanik et al. (2020) who derived new MOST (Monin Obukhov Similarity Theory) SCFs (Stability Correction Functions) for momentum $\psi_m(\zeta) = -3(a_m/b_m)[(1 + b_m \cdot \zeta)^{1/3} - 1]$ and heat $\psi_h(\zeta) = -Pr_0(a_h/b_h)\ln(1 + b_h \cdot \zeta)$ as a function of $\zeta = z/L$ ($0 \leq \zeta < 100$), where z is height and L is the Obukhov length. $Pr_0 = 0.98$ is the neutral-limit turbulent Prandtl number and the constants are: $a_m = 5.0$, $b_m = 0.3$, $a_h = 5.0$, and $b_h = 0.4$. The new SCFs resulted from an optimization to SHEBA (Surface Heat Budget of the Arctic Ocean) data (Uttal et al. 2002) considering their functional form, values of constants, and dependence of ζ from the bulk Richardson number (Ri_b).

Furthermore, Gryanik and Lüpkes (2018) developed a new non-iterative scheme to determine transfer coefficients for momentum $C_d(Ri_b, \epsilon_m, \epsilon_t)$ and heat $C_h(Ri_b, \epsilon_m, \epsilon_t)$ (where $\epsilon_m = z/z_0$ and $\epsilon_t = z/z_t$ are roughness parameters), which can be used with the above SCFs. It turned out that relative to SHEBA data, the new transfer coefficients are superior to those of previous schemes over sea ice (Fig. 8). They can be part of a package of new non-iterative parameterizations based

on measurements in different regions on Earth as well (Gryanik et al. 2021; Gryanik and Lüpkes 2022). The new improved stability functions have been implemented in HIRHAM5. Roughness lengths were adjusted to mean values derived from SHEBA ($z_0 = 3.3 \times 10^{-4}$ m for momentum and $z_t = 6.6 \times 10^{-5}$ m for heat). In simulations of wintertime conditions, the significant impact of these changes was shown through modifications to the regional circulation, wind, and near-surface turbulent fluxes (Schneider et al. 2022).

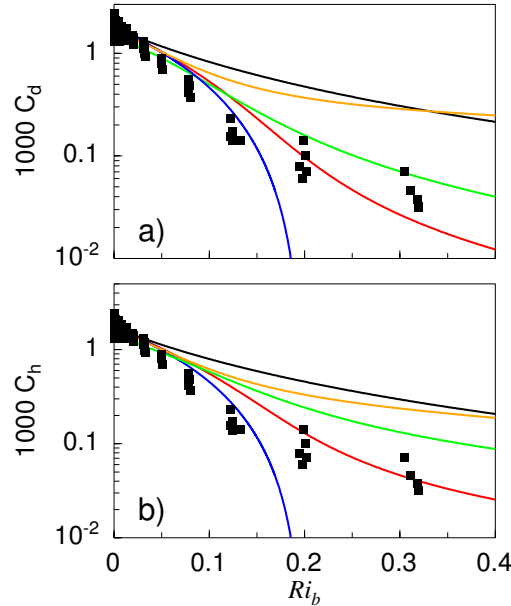


FIG. 8: Transfer coefficients for momentum C_d and heat C_h as a function of the bulk Richardson number Ri_b . Solid lines show 10 m values obtained with different parameterizations using surface roughnesses as given in the text. The curve notation is as follows: Black: Louis (1979); orange: Beljaars and Holtslag (1991); green: Grachev et al. (2007); red: new development of Gryanik et al. (2020); blue: Businger et al. (1971) and Dyer (1974). Black squares show SHEBA data obtained in the surface layer at different heights.

In a warmer Arctic with thinner sea ice, the number of leads is likely to increase. It was confirmed within $(\mathcal{AC})^3$ that even though leads occupy only a small areal fraction, they exert a large impact on the regional temperature, stability over sea ice, and surface fluxes (Chechin et al. 2019). Therefore, a new parameterization of convective plumes and related processes over leads of different widths has been established within $(\mathcal{AC})^3$ (Michaelis et al. 2020, 2021). It is applicable in plume-resolving, computationally inexpensive models with much coarser resolution than LES, which enables extensive scenario studies. It was shown that the impact of leads on the surface fluxes over a typical domain of a grid cell of a climate model depends critically on geometric lead

parameters (e.g., lead width). Such subgrid-scale characteristics of leads are not considered in an individual model grid cell (Michaelis and Lüpkes 2022). Furthermore, a new conceptual model of the ABL coupled to sea ice in the presence of leads was proposed by Chechin et al. (2019) describing analytically the ABL warming due to leads as a function of wind speed. In particular, the new model highlights and explains the role of leads in the formation of decoupling between the sea ice surface and the ABL temperatures, being a step forward compared to earlier studies (Lüpkes et al. 2008). Another new result of Chechin et al. (2019) was the finding that the threshold value subdividing different stability regimes in the environment of leads is a function of the lead fraction. Furthermore, it was shown by Chechin et al. (2019) that those regimes agree well with data from Russian drifting stations and that there is a clear connection between the net terrestrial surface radiative energy fluxes and wind speed.

b. Upper Ocean Effects (Brown in Fig. 2)

Closely linked to the surface albedo effect are consequences for the upper ocean biological activity that partly feedback to components of the system. Some examples of these interactions studied within (\mathcal{AC})³ are given in Subsections *b–1. Cryosphere-Ocean-Atmosphere Interactions*, and *b–2. Ocean Biogeochemistry*.

b–1. Cryosphere-Ocean-Atmosphere Interactions: Feedbacks and Coupled Processes

A positive feedback mechanism involving wind stress, sea surface temperature, and sea ice in the Nordic Seas was investigated during (\mathcal{AC})³ using a fully coupled Earth system model (Kovács et al. 2020). It was shown that an anticyclonic wind anomaly causes a strong surface cooling in the Greenland Sea, which is mostly due to the drift of sea ice. The cooling reduces the net surface heat flux to the atmosphere and increases sea-level pressure. The pressure gradients cause southerly winds that are comparable to the prescribed forcing anomalies, suggesting a positive feedback. In another study within (\mathcal{AC})³, Metzner et al. (2020) investigated the role of changes in the Arctic Ocean cold halocline for ocean heat transfer from the ocean to the atmosphere. The cold halocline is a stable layer that separates warm Atlantic water from the overlying cold mixed layer. Previously, observational studies had suggested that the cold halocline is retreating (Steele and Boyd 1998; Polyakov et al. 2017). Based on CMIP5 model results, we found within (\mathcal{AC})³ that in future

climate projections, events, in which warm Atlantic water is no longer separated from the ocean mixed layer, become more frequent, facilitating an increased surface heat flux from the Arctic Ocean to the atmosphere during winter. Furthermore, in the Fram Strait, part of the circulation of Atlantic water and its subduction was found to be dominated by eddies, and therefore prone to changes caused by atmospheric forcing (Hofmann et al. 2021).

b–2. Cryosphere and Ocean Biogeochemistry: Impact on Trace Gases & Aerosol Particles

Temporal trace gas changes are associated with sea ice trends. As an example, a positive tropospheric BrO trend of about 1.5 % per year during polar spring was identified within (\mathcal{AC})³, which appeared to be correlated with an increase in FYI, at the expense of MYI (Bougoudis et al. 2020). Spatial trend patterns of BrO appeared to vary, indicating that local factors such as the amount of blowing snow and meteorological parameters play an important role.

Clear indications for local marine sources of biogenic INPs were found during airborne (Hartmann et al. 2020) and ship-based (Hartmann et al. 2021) filter sampling within (\mathcal{AC})³. Efficient biogenic INPs were also found in fog droplets (Hartmann et al. 2021). Further data have shown that Arctic INPs feature a seasonal cycle with highest concentrations in summer and lowest in winter (Wex et al. 2019). In the laboratory, the INPs nucleated ice at temperatures as high as -7.5°C (Hartmann et al. 2019, 2020) or even up to -5°C (Wex et al. 2019). Prior to these studies done within (\mathcal{AC})³, it had generally been assumed that Arctic INP concentrations are low (Loewe et al. 2017). In general, Arctic INPs are grossly unexplored, and therefore still provide a large source of uncertainty for understanding Arctic clouds (Morrison et al. 2012). The new results achieved within (\mathcal{AC})³ show that ice nucleation at high freezing temperatures can also occur for Arctic clouds in summer.

A closure study concerning INP number concentrations in the SML (Sea Surface Microlayer) and the atmosphere suggested that INPs need to be significantly enriched during transfer from the SML into the atmosphere, meaning that INPs need to be emitted preferentially, compared to sea salt, to explain observed atmospheric INP concentrations based on sea spray production (Hartmann et al. 2021). To elucidate the chemical links between INPs and marine carbohydrates, an analysis method to detect free and combined carbohydrates in saline samples was developed (Zeppenfeld et al. 2020). Measurements revealed that glucose may serve as a biological INP tracer in the

central Arctic Ocean. In sea water, phytoplankton composition and its overall abundance show a linkage to glucose, which is likely formed or released together with biogenic INPs. The SML of the MIZ (Marginal Sea Ice Zone) and aged melt ponds are particularly enriched in glucose and INPs (Zeppenfeld et al. 2019). Hence, there are strong indications that the MIZ and melting sea ice environments represent local sources of marine INPs. Supplementary investigations of ice core samples have shown that INP concentrations in the Arctic seem not to be affected by anthropogenic pollution (Hartmann et al. 2019).

Aerosol particles acting as CCN are important for liquid water cloud processes. Hartmann et al. (2021) examined CCN and INP concentrations in a case study and did not find a correlation between these two types of particles. In a further study, new particle formation events were observed in the summertime Arctic, which were shown to increase the background CCN concentrations (Kecorius et al. 2019).

c. Local Atmospheric Processes (Green in Fig. 2)

Local processes and feedback mechanisms take place at a fixed location; their causes and impact are mostly restricted to the same place. In this section we focus on local phenomena caused by clouds (Subsections c–1 to c–3) and precipitation (Subsection c–4), which consider key aspects within $(\mathcal{AC})^3$ in general (Wendisch et al. 2019).

c–1. Clouds: Representation by Models

Clouds were analyzed in the ECHAM6 GCM in combination with data from the CALIPSO cloud-aerosol lidar and a satellite simulator (Kretzschmar et al. 2019). As expected, the evaluation pointed to the Wegener-Bergeron-Findeisen (WBF) process as a key determinant of the life cycle of Arctic mixed-phase clouds. Corrections of the representation of the WBF were required to obtain an improved agreement between satellite data and model results in the Arctic. To further enhance the cloud representation in regional Arctic climate models, more realistic, observation-tied modeling of CCN activation (Kretzschmar et al. 2020; Mech et al. 2020), and the use of appropriate INP concentrations (Sedlar et al. 2020) were identified as crucial factors.

Targeted LES were designed to explore the interaction of mixed-phase clouds with the large-scale flow (Neggers et al. 2019; Egerer et al. 2021). Furthermore, Lagrangian model configurations were

adopted that follow the clouds as embedded in warm/moist air mass intrusions, constrained by measurements collected during PASCAL. We find that entrainment deepening driven by liquid cloud top cooling occurs persistently, but varies very little and cannot fully explain the effective mixed layer deepening. In contrast, large-scale subsidence acts much more as a control on mixed layer evolution. It is much more episodic, including strong subsidence events that are even capable of causing cloud collapse (Neggers et al. 2019). This behavior can well be captured by idealized bulk mixed layer model approaches.

c-2. Clouds: Impact of Surface Conditions and Air Mass Properties

In general, and not surprisingly, in-situ and remote sensing observations conducted during (\mathcal{AC})³ clearly emphasized that the cloud properties were significantly impacted by surface conditions and air mass characteristics. More specifically, we could show that over sea ice, the total water path, and the mean droplet number and mass concentrations were lower, and the droplet sizes smaller than over open ocean (Mioche et al. 2017; Mech et al. 2019; Ruiz-Donoso et al. 2020). In addition, airborne radar measurements verified that clouds over sea ice were of a lower vertical extent with more frequent but rather low amounts of precipitation, as compared to clouds over open ocean (Mech et al. 2019). During ACLOUD, mixed-phase clouds and precipitation were not observed at temperatures below -14°C . Over the MIZ in particular, they were not observed at temperatures below -10°C . Higher concentrations of small droplets were encountered during southerly air flows, which were characterized by higher CCN concentrations, compared to clouds associated with cleaner air masses originating from the North (Wendisch et al. 2019).

Dedicated LES experiments for selected ACLOUD flights and respective sensitivity tests revealed that CCN concentrations in the air mass significantly affect the efficiency of radiatively driven entrainment in warming the boundary layer. The response in the thermal inversion strength plays a key role in this impact (Chylik et al. 2021). Measurements of cloud droplet residuals, sampled in clouds by means of a counterflow virtual impactor (Ehrlich et al. 2019), and aerosol particles above and below clouds have indicated whether the cloud forming particles were linked to the surface layer below cloud base, or to the free troposphere above the cloud top inversion (Wendisch et al. 2019). The latter was the case for clouds over sea ice, while above the open ocean cloud-forming particles likely originated from below the cloud. Whether this pattern is directly linked to the

emission of aerosol particles at the surface or indirectly caused by the different thermodynamic and turbulence profiles over both surfaces is still unclear. However, the turbulence measurements during the (\mathcal{AC})³ airborne campaigns verified the important role of cloud-generated turbulence in the ABL over sea ice (Wendisch et al. 2019; Chechin et al. 2022). Additionally, in-situ observations identified larger cloud particle residuals over open ocean with smaller ones over sea ice, which further indicates different pathways for aerosol particles, feeding the cloud from below and/or above the cloud. Further investigations of the influence of surface-coupling showed that for cloud top temperatures higher than -10°C , surface-coupled clouds contained ice more often than clouds that were decoupled from the surface (Griesche et al. 2021). This suggests an influence of near-surface aerosol particles in the process of heterogeneous ice formation for Arctic ABL clouds at weakly super-cooled temperatures.

Humidity inversions just above cloud top have been detected by the BELUGA system by Egerer et al. (2021) with a higher vertical resolution than provided by earlier radiosonde studies (Naakka et al. 2018). Dedicated LES experiments were designed, based on the method explored by Neggers et al. (2019), to accompany the BELUGA measurements and to function as a virtual laboratory for investigating impacts of humidity inversions on clouds below.

c-3. Clouds: Interaction with Atmospheric Energy Fluxes

Cloud radiative impacts typically drive variability in the overall surface energy budget (SEB⁴), where other terms of the SEB most often respond to the radiative energy fluxes. To first order, cloud radiative effects control the surface skin temperature, which in turn affects the near-surface stratification and, thus, the sensible heat flux. The vertical sensible heat flux typically acts to mitigate variability in surface radiative energy fluxes and, thus, feeds back on the near-surface air temperature. Collectively, as the partitioning of radiative and turbulent heat fluxes constrains the surface temperature, this also determines the conduction of heat through the sea ice from the warm ocean below. MOSAiC observations have shown that the winter surface temperature was $8\text{--}10^{\circ}\text{C}$ higher when liquid water clouds were present versus when they were not (Shupe et al. 2022). Similarly, surface sensible and conductive heat fluxes were each significantly diminished under cloudy skies. The sensible heat flux was 10 W m^{-2} less, and the conductive heat flux is also up to

⁴The surface energy budget (SEB) is generally defined as the net (downward minus upward) energy flux density of the radiative, turbulent sensible, latent heat, and conductive heat fluxes. It is given in units of W m^{-2} .

10 W m^{-2} less. The magnitude of these impacts depends on many details, including ice thickness, snow depth, solar radiative energy input, and others.

It was shown that state-of-the-art Arctic regional models are, in principle, able to represent critical observed transitions of the SEB. However, the across-model spread of the results can be large (Sedlar et al. 2020), which is mainly related to the different treatments of clouds and cloud-radiation interactions. In particular, models struggle with the proper representation of the cloud phase partitioning and vertical distribution of cloud LWC (Liquid Water Content), compared to observations (Inoue et al. 2021; Kretzschmar et al. 2019, 2020).

(\mathcal{AC})³ airborne measurements close to and over the MIZ identified four distinct modes of near-surface terrestrial net irradiances below clouds (Wendisch et al. 2019; Kretzschmar et al. 2020; Stapf 2021), distinguishing low versus high surface albedo, and cloud-free versus opaquely cloudy states (Fig. 9). This conceptual framework generalizes the previous classification into two typical atmospheric states in the Arctic (Shupe and Intrieri 2004; Stramler et al. 2011; Graham et al. 2017b). In addition, seasonal influences of surface and thermodynamic properties on the mode structure have been revealed. During AFLUX (spring), strong surface temperature gradients between sea ice and the open ocean (up to 25 K) were observed, while during the second half of ACLOUD (melting period during early summer) smaller temperature gradients of only up to 6 K were found. A warming surface causes an increase of upward terrestrial radiation meaning a more negative net (downward minus upward) irradiance (increased loss of terrestrial radiation at the surface, radiative cooling), because more upward terrestrial radiation is emitted by the surface. Thus, the cloud-free modes over sea ice and open ocean differ strongly in response to the large horizontal temperature gradient prevailing during AFLUX (Fig. 9a). For opaquely cloudy conditions, cloud base temperature is crucial, since it determines the downward terrestrial radiation. Cloud base temperature is approximately the same when over sea ice or adjacent open ocean, leading to similar downward irradiance. However, the upward irradiance is significantly higher over the warmer open ocean compared to the sea ice, resulting in more negative values of terrestrial net irradiance (increased loss of terrestrial radiation) over the ocean than over the sea ice during AFLUX. During ACLOUD, with a much smaller gradient of surface temperature, the corresponding cloud-free and opaquely cloudy modes differ only slightly over sea ice and open ocean (Fig. 9b). This last

statement is true for terrestrial radiative balance, but not for solar, which could be the dominant term of the total (solar plus terrestrial) net irradiances depending on sun angle.

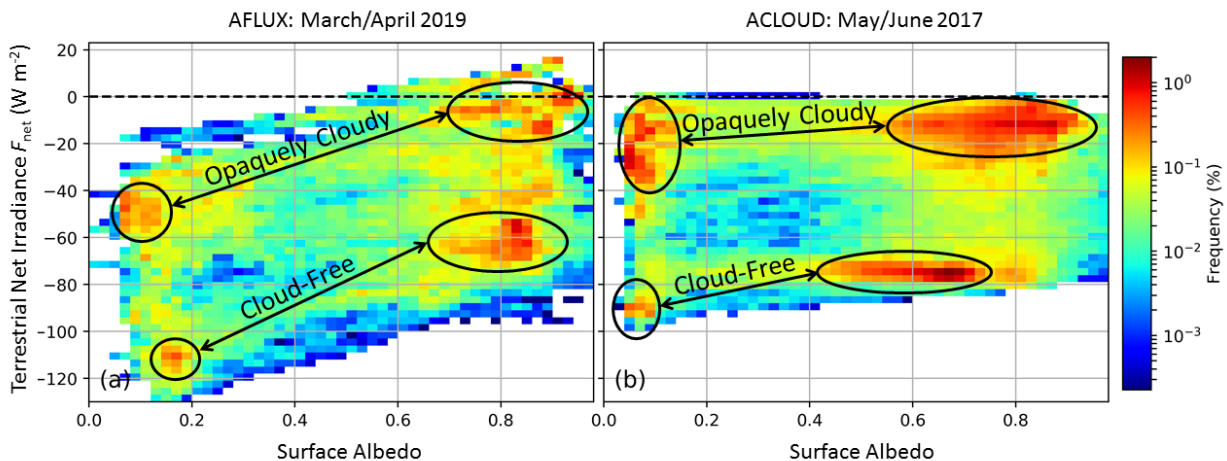


FIG. 9: Joint two-dimensional histogram of frequency distribution of terrestrial net irradiance (measured below clouds) as a function of all-sky surface albedo observed during (a) AFLUX and (b) ACLOUD. Two modes (cloud-free and opaquely cloudy) become obvious over both open ocean (low surface albedo) and sea ice (high surface albedo). The Figure is taken from Stapf (2021).

Simulations of terrestrial net irradiances at cloud-system-resolving kilometer-scale resolutions were conducted using the ICON model and compared with the airborne observations during ACLOUD (Kretzschmar et al. 2020). The simulations represented the observed four-mode radiative structure close to the surface comparatively well if the measured surface albedo was implemented into ICON (Wendisch et al. 2019). Several model deficiencies, however, were identified when investigating the cloud microphysical state in detail. The simulations were improved when the cloud droplet activation scheme was revised, using an observations-tied profile of CCN and a representation of the turbulence impact on cloud-scale updraft speeds (Kretzschmar et al. 2020).

Depending on cloud properties, the season of the year, and surface conditions, Arctic clouds may warm or cool the surface. To quantify the cloud effect on radiative energy fluxes the concept of the cloud radiative forcing (CRF) was applied during ($\mathcal{A}\mathcal{C}$)³. The few available observation-based

retrievals of the CRF of Arctic clouds were significantly extended by continuous, ground-based and ship-borne observations, and in-situ airborne measurements in different seasons (Barrientos-Velasco et al. 2020; Ebell et al. 2020; Stapf et al. 2020, 2021; Stapf 2021). From the continuous observations at the AWIPEV research base, the surface CRF was calculated over more than two years (Ebell et al. 2020). The results confirmed a negative CRF (cooling effect of clouds) in summer and a warming by clouds from September to April/May with an annual positive CRF of 11 W m^{-2} . Liquid-containing clouds were found to be the largest contribution to the CRF. Additionally, the CRF was estimated considering ship-borne and satellite remote sensing observations for the summer of 2017, using data from PASCAL (Griesche et al. 2020). The results indicated a cooling effect of about -9 W m^{-2} (Barrientos-Velasco et al. 2022). Airborne observations of the CRF covered open ocean and sea ice surfaces, as well as the MIZ (Stapf et al. 2020, 2021; Stapf 2021). Fig. 10 illustrates the warming effect of clouds over sea ice (highly reflecting surface) and the cooling over ocean (low surface albedo) as derived from all ACLOUD observations. The solar CRF depended strongly on the interaction of clouds and the surface albedo (Jäkel et al. 2019; Stapf et al. 2020). Over snow and sea ice surfaces, the estimated average solar cooling by clouds almost doubles if this interaction is taken into account. This emphasizes the importance of realistic surface albedo parameterization in models.

c-4. Precipitation: Radar Observations and Regional Modeling

Precipitation, in particular snowfall, is a critical component of the Arctic climate system influencing the hydrologic cycle and surface energy fluxes through impacts on surface albedo and sub-surface conduction. During $(\mathcal{AC})^3$, innovative retrieval algorithms converting cloud radar measurements to snowfall rate were developed, based on in-situ and remote sensing measurements (Schoger et al. 2021). Furthermore, the skill of five reanalyses and the regional climate model HIRHAM5 in simulating precipitation associated with atmospheric river cases during the ACLOUD/PASCAL campaign was studied (Viceto et al. 2022). The total precipitation amounts were similar, however, the discrimination of the precipitation phase showed major differences. Also, the seasonal and regional distribution of snowfall in HIRHAM5 simulations over the period of 2007-2010 were evaluated in two ways: using the CloudSat retrieval (classical approach), and applying the forward operator PAMTRA (von Lerber et al. 2022). The classical retrieval approach

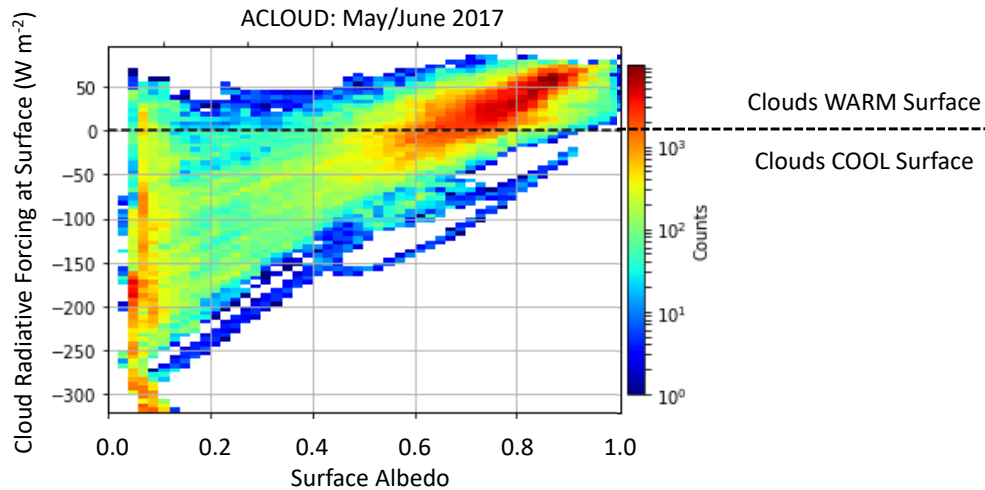


FIG. 10: Two-dimensional histogram of frequency distribution of CRF (cloud radiative forcing) as a function of surface albedo derived from ACLOUD observations. Two cloud modes become obvious over open ocean (low surface albedo) and sea ice (high surface albedo). The Figure is adapted from Stapf (2021).

reveals that HIRHAM5 is much closer to the mean snowfall rate than ERA-Interim, and the model reproduces the surface snowfall associated with specific weather patterns as observed by CloudSat. The only exception is the northerly direction typically occurring during marine cold air outbreaks where HIRHAM5 seems to underestimate the associated snowfall.

d. Arctic – Mid-latitude Linkages (Yellow in Fig. 2)

Arctic amplification is not only dependent on local physicochemical and biogeochemical processes and their non-linear feedbacks, but is also largely affected by a hierarchy of regional and global changes of atmospheric composition and dynamics, as well as by the related meridional and vertical transport of energy and matter in the atmosphere, ocean, and cryosphere. These transports into and out of the Arctic, which change over time due to internally generated and externally forced changes in large-scale atmospheric and oceanic variability patterns, link the Arctic with the mid-latitudes and vice versa. Here we focus on temporal trends and processes, which are

related or possibly caused by meridional transports in the atmosphere. They include *d-1. Water Vapor and Clouds*, *d-2. Precipitation*, and *d-3. Aerosol Particles*. Furthermore, we look at *d-4. Stratospheric Pathway, Ocean Heat Transport, and Atmospheric Cyclonic Circulation*.

d-1. Water Vapor and Clouds: Temporal Trends

(\mathcal{AC})³ has shown that a set of factors, including increasing temperature and moisture advection, increasing sea surface temperature, and reduced sea ice extent have caused an overall increasing trend of IWV averaged over the time period of 1979-2016 and the central Arctic ($\geq 70^\circ$ N) during all seasons (Rinke et al. 2019b). Recently, a shift of the maximum IWV trend from summer to fall was observed. This phenomenon is related to an accelerated increasing trend of IWV observed over the Barents and Kara Seas associated with the sea ice retreat, and respective consequences on warming and atmospheric circulation changes in that region. Notably, the Arctic-wide moistening trend is also reflected over large parts of the central Arctic Ocean in fall and winter (Rinke et al. 2019b), as well as in local long-term observations at the AWIPEV research base in Svalbard (Barthlott et al. 2017; Kulla and Ritter 2019; Nomokonova et al. 2020). This moistening has been linked to an increased occurrence and persistence of storms (Rinke et al. 2017; Zahn et al. 2018) that transport moist and warm air into the Arctic and cause a distinct winter warming of the Svalbard and North Pole regions (Dahlke and Maturilli 2017; Graham et al. 2017a). The enhanced moisture advection via the North Atlantic pathway has further been attributed to changed atmospheric circulation patterns (Mewes and Jacobi 2019, 2020), namely an enhanced occurrence of the Scandinavia/Ural high pressure blocking in early winter, and to sea ice retreat in the Barents and Kara Seas (Dahlke and Maturilli 2017; Crasemann et al. 2017). The moistening can have far-reaching impacts. For example, higher relative humidity was identified as a major factor for the growth of polar lows (Radovan et al. 2019). However, from the analysis of numerous satellite-based IWV products, strong differences of monthly mean IWV have been found in summer, likely due to the challenge of representing the complex and changing surface characteristics within the retrieval algorithms (Crewell et al. 2021). This is in line with the identified large differences in the IWV trend across reanalyses over the central Arctic Ocean in summer (Rinke et al. 2019b).

Ground-based observations at the AWIPEV research base hint at an increase of cloud occurrence, LWP (Liquid Water Path), and IWP (Ice Water Path) in all seasons (Nomokonova et al. 2020).

Using a new retrieval algorithm (Nakoudi et al. 2021b), the long-term analysis (2011-2020) of data collected at AWIPEV revealed that in winter and spring cirrus clouds are thicker and seem to appear more frequently (Nakoudi et al. 2021a). From the preliminary analysis of satellite data from previous research outside (\mathcal{AC})³, it appears that an increase in cloud LWP has resulted in a positive trend in COT for the liquid phase of 2.8 % per decade and a negative trend in COT for the ice phase of -6.1 % per decade (Lelli et al. 2022).

d-2. Precipitation: Atmospheric Rivers

Atmospheric rivers (ARs) represent filament structures of enhanced vertically integrated, horizontal moisture transport, which are found responsible for a majority (up to 80 % in winter) of the poleward moisture transport into the Arctic (Nash et al. 2018). This high percentage is despite their rare occurrence globally and even more rarely reaching the Polar regions (Guan and Waliser 2019; Wille et al. 2021). ARs are often associated with intense precipitation and they can trigger sea ice and Greenland ice sheet surface melt events (Neff 2018; Box et al. 2022). Significant uncertainties exist in the detection of the ARs particularly in the Arctic (Rutz et al. 2019). Within (\mathcal{AC})³, observations at the AWIPEV research base in Ny-Ålesund were combined with satellite-derived data, models, and state-of-the-art reanalysis products to study ARs (Bresson et al. 2022; Viceto et al. 2022). The regional climate model HIRHAM5 and the Limited-Area Mode (LAM) ICON model were used to study specific AR events during the ACLOUD and PASCAL campaigns. In order to identify AR events, a new polar-specific algorithm by Gorodetskaya et al. (2020) was adapted to the Arctic and compared to the global algorithm by Guan and Waliser (2019). The analyzed cases highlighted the importance of the Atlantic AR pathway in winter, but also its shift eastward (towards Siberia) in spring and summer. Compared to observations during these events, it was demonstrated that model simulations with high horizontal resolution (down to 3 km) result in an improved representation of the spatio-temporal AR structure and its signature in the temperature, humidity, and wind profiles relative to global simulations and the ERA5 reanalysis (Bresson et al. 2022). Results also revealed the important role of ARs originating in western Siberia for influencing Svalbard and Greenland in May-June (Viceto et al. 2022). Tropospheric humidity profile measurements derived from radiosondes showed the AR-related increase in low-level moisture, sometimes topped by a dry layer above, which were not well captured in HIRHAM5, while

ICON-LAM sufficiently represented the fine vertical structure and its evolution (Bresson et al. 2022; Viceto et al. 2022). An important feature of the analyzed AR events was a transition from rainfall over the land areas to preferentially snowfall over the sea ice during a May AR event, and a dominance of rainfall during the June events (Viceto et al. 2022). Furthermore, the significant impact of the ARs on the surface radiative energy fluxes has been quantified (Bresson et al. 2022).

d-3. Aerosol Particles: Temporal Changes, Transport, Radiative Effects, and Global Simulations

The ACLOUD and PAMARCMiP airborne campaigns, conducted in the European Arctic, confirmed higher BC (Black Carbon) number concentrations in spring, compared to lower values in early summer (decrease by a factor of five, almost equally at all altitudes), which is similar to observations performed in the Canadian Arctic (Schulz et al. 2019). These seasonal differences are mainly controlled by transport patterns and emission sources (Willis et al. 2019), and also by cloud processes in the ABL (Wendisch et al. 2019). Preliminary analyses of existing satellite data in the framework of (\mathcal{AC})³ have revealed a long-term negative trend in aerosol optical thickness over the Arctic Ocean between -12 % to -13 % per decade (1981-2020), which is attributed to both the reduction of the transport of tropospheric aerosol particles and their precursors from Europe and North America and the reduction of stratospheric aerosol particles. However, an increase of large Northern Hemisphere wildfires in recent years has provided large smoke layers over the central Arctic up to the stratosphere (Ohneiser et al. 2021). The year-to-year variation of biomass burning activities also likely affected BC amounts in the Arctic troposphere in spring (Ohata et al. 2021). In general, and aside from lack of satellite coverage at very high latitudes, one of the main challenges in the retrieval of atmospheric aerosol (and cloud) properties over the Arctic ocean from spaceborne passive microwave measurements is sea ice coverage and melt ponds on sea ice. (\mathcal{AC})³ made some progress in considering highly reflective surfaces in the aerosol retrievals (Mei et al. 2020b,c), although the problem is not fully solved yet.

During PAMARCMiP, aerosol particles transported over long distances were observed above the Fram Strait and Ny-Ålesund. They consisted of a mixture of industrial pollution and biomass burning particles (Nakoudi et al. 2020). In a unique approach, the radiative forcing of these aerosol particle plumes was estimated taking into account their modifications during the transport. As a result, although different aerosol size distributions were derived over Fram Strait and over

Ny-Ålesund, the solar aerosol radiative forcing was similar for both locations, ranging between 4.4 W m^{-2} and 4.9 W m^{-2} . Furthermore, the dependence of the radiative effects of BC on the mixing state, vertical distribution, surface albedo, and cloud properties was systematically investigated within $(\mathcal{AC})^3$ on the basis of measured data and not purely based on simulations (Kodros et al. 2018; Zanatta et al. 2018; Donth et al. 2020). In a case study, retrievals of aerosol microphysical properties were used to estimate the radiative impact of a specific biomass burning event (Ritter et al. 2018). In addition, mass concentrations of BC particles originating either from long-range transport or local emission and then deposited at the ground and embedded in surface snow layers were measured during PASCAL; the observed values ranged between $2\text{--}10 \text{ ng g}^{-1}$. Their absorption effect caused a local solar radiative warming at the surface, which was estimated by radiative transfer simulations to be up to 0.7 W m^{-2} (Donth et al. 2020). However, Zanatta et al. (2021) have recently discovered that the BC mass detection efficiency of the respective instrument, the single particle soot photometer, drastically drops with increasing sea salt content during snow sample analysis. Therefore, the previously determined BC mass concentrations in surface snow layers might be seriously underestimated and with this their solar radiative warming as well. The onset of melting in spring and early summer led to an accumulation of BC within the snow layer at the surface, yielding BC mass concentrations exceeding 10 ng g^{-1} , probably even higher due to the exposure of deeper snow layers with higher BC loading. Although, the radiative effects of BC in snow and atmosphere are well documented from model simulations (Warren and Wiscombe 1980; Flanner 2013), the quantitative influences of BC on the radiative forcing of the atmosphere-surface system, based on measured BC concentrations within both, the atmosphere (especially the high concentration in spring), and the surface snow is still unclear.

Within $(\mathcal{AC})^3$, global aerosol-climate modeling has investigated the controls of seasonal and vertical BC variability, as well as key uncertainties limiting the accuracy of model estimates of Arctic BC and its radiative effects (Schacht et al. 2019). Available literature shows that models tend to underestimate BC in the lower Arctic troposphere, but are often biased high at altitudes above 500 hPa (Sand et al. 2017; Lund et al. 2018). Schacht et al. (2019) introduced improved emission assumptions into the modeling, which helped to reproduce observations with 25 % higher BC burden, while an optimized representation of aerosol aging and wet removal led to 10 % lower high-altitude loadings. Schacht et al. (2019) also found values of top of atmosphere (TOA) BC

radiative forcing of $+0.31 \text{ W m}^{-2}$, and a BC-in-snow albedo effect of $+0.12 \text{ W m}^{-2}$, averaged over the Arctic ($> 60^\circ \text{ N}$) for years 2007-2018, which places this study in the upper range of recent climate-model estimates (Sand et al. 2017; Gliß et al. 2021).

d-4. Stratospheric Pathway, Ocean Heat Transport, and Atmospheric Cyclonic Circulation

Arctic amplification and related sea ice decline has an impact on the large-scale atmospheric circulation and energy transport. A tropospheric pathway expressed by more frequent occurrence of high pressure blocking situations over Scandinavia and northern Eurasia in early winter (Crasemann et al. 2017) initiates a stratospheric pathway with enhanced upward propagation of wave energy and momentum weakening the stratospheric polar vortex (Romanowsky et al. 2019). The subsequent downward propagation of these stratospheric circulation anomalies contributes to persistent negative NAO (North Atlantic Oscillation) anomalies in late winter (Jaiser et al. 2016). This dynamical pathway is considered as most robust (Cohen et al. 2020), but it is still missing in many climate models (Smith et al. 2022). An improvement of the modeling of this stratospheric pathway by including interactive stratospheric ozone chemistry into GCMs was achieved within (\mathcal{AC})³ (Romanowsky et al. 2019).

Two (\mathcal{AC})³ model studies found evidence for positive atmosphere-sea-ice-ocean feedback processes triggered over the North Atlantic sector, which is the key region for oceanic heat transport into the Arctic (Akperov et al. 2020; Kovács et al. 2020). Combined with atmospheric changes and winter sea ice decline, an increased Atlantic northward ocean heat transport was observed via the strengthening and warming of the Atlantic water inflow. Model experiments indicate that an anomalously high Atlantic water inflow through the Barents Sea opening in winter was associated with a cyclonic circulation anomaly and sea ice reduction in the Barents Sea region, which can lead to decreased atmospheric stability and increased wind shear in the lower troposphere, providing favorable conditions for cyclogenesis (Akperov et al. 2020). These shifts may lead to further increasing Atlantic water inflow, suggesting a potential positive regional feedback.

Further model experiments have shown that also changes in the strength of the cyclonic circulation over the Nordic Sea in winter can potentially trigger positive feedback mechanisms (Kovács et al. 2020). Such circulation changes may cause significant anomalies in sea ice cover and sea surface temperature, especially in the Greenland Sea, which may lead to exceptional ocean-air heat fluxes

modifying the atmospheric stability and possibly amplifying the initial wind anomaly. Due to more favorable conditions for cyclogenesis, cyclones might penetrate further to the North and reach the central Arctic with important implications for further reduction of sea ice through a shifted sea ice edge, reduced sea ice growth, ice break ups in winter, and amplified sea ice retreat in the subsequent summer. The changed baroclinic cyclones impact planetary wave patterns as well and thereby introduce some degree of unpredictability of large-scale atmospheric waves into climate models (Cohen et al. 2020).

5. Where do we go from here?

To understand and project the interlinked effects of atmospheric and surface processes and feedback mechanisms on Arctic amplification, the many pieces of the Arctic climate puzzle obtained by $(\mathcal{AC})^3$ so far, and those to be achieved in the future of this project, must be assembled. This synthesis will be achieved by two efforts: (i) Enabling models to more realistically represent the relevant processes across scales and use them for sensitivity studies to quantify the relative importance of the processes driving Arctic amplification, and (ii) Combining and integrating observational and modeling activities focusing on major drivers of Arctic amplification. Effort (i) will continuously be pursued within $(\mathcal{AC})^3$ by anchoring models in reality using state-of-the-art observations, and by further improving parameterizations and process representations. Activities with regard to effort (ii) are currently being intensified within $(\mathcal{AC})^3$ by focusing on research of the four following major crosscutting processes and drivers of Arctic amplification.

a. Lapse Rate Feedback

The usually low ABL height promotes an amplified near-surface warming and a rather muted free-tropospheric heating in the Arctic, which determines the lapse rate feedback. This mechanism is linked to surface energy fluxes, vertical mixing, clouds, radiation, and large-scale advection. First results on the lapse rate feedback underline the importance of the surface fluxes in particular where sea ice retreats. They show strong increases in the lapse rate response to warming in the past 40 years, which may imply opportunities for thorough model evaluation.

Key questions that are being pursued in $(\mathcal{AC})^3$ to quantitatively investigate the processes driving the lapse rate feedback, to verify and improve its representation in climate models exploiting

observations, and to quantify its contribution to Arctic amplification are: (i) Which processes determine the surface energy budget? (ii) How does vertical mixing and the inversion strength change in the Arctic, both spatially and temporally? (iii) Which mechanisms govern advective heating and cloud-top radiative cooling? (iv) How does the free-tropospheric temperature change?

b. Coupled Surface-Atmosphere Processes

Coupling between the atmosphere and surface (snow cover, sea ice, open ocean or land) strongly constrains surface energy fluxes. For example, the transition from large sea ice cover, through fractured sea ice (leads, polynyas) to open (sea ice-free) ocean, involves dramatic changes in radiative and turbulent energy fluxes. To consider these systems, three major questions will be addressed: (i) What is the influence of changing surface types (e.g., open-water leads, rough/smooth, warm/cold, biochemically active/inactive surfaces) in the Arctic on near-surface air temperatures, turbulent and radiative energy fluxes, and air mass transformation in the different Arctic sub-regions? (ii) How do changing Arctic surface properties affect the emission of marine aerosol precursors as a source of atmospheric particles, and aerosol-cloud interactions in the Arctic? (iii) Which degree of surface heterogeneity must be represented in models?

c. Arctic Mixed-Phase Clouds and their Representation in Models

To better understand the mixed-phase cloud persistence as well as their macro/microphysical and radiative properties on various scales, data collected during (\mathcal{AC})³ (ground-based, airborne, ship-based, satellite observations) from different regions (Ny-Ålesund, Eurasian, western and central Arctic) will be analyzed in a synergistic way. Combining the observations with simulations will help to assess cloud parameterizations across the Arctic. For this purpose, the following major questions will be tackled: (i) How do surface and synoptic conditions and air mass transformations influence the representation of mixed-phase clouds in coarse and high-resolution models? (ii) What is the impact of changes in cloud phase on cloud radiative effects? (iii) How do aerosol-cloud-turbulence interactions influence the properties and evolution of Arctic aerosol particles and Arctic mixed-phase clouds?

d. Air Mass Transport and Transformation

The interplay between warm/moist air intrusions into the Arctic and cold air outbreaks is decisive for the overall energy budget of the Arctic. The air mass transformations along their path over different surfaces are challenging to model. Deficiencies in the model representation of the development of clouds and precipitation both in respect to their positioning and amount have been identified. Within the recent HALO–(\mathcal{AC})³ airborne campaign, successfully completed in March/April 2022 (Wendisch et al. 2021), dedicated flight patterns have been flown to map the spatio-temporal development of pronounced air mass transports to provide reference cases for Lagrangian-like investigations. In addition, anomalously strong moisture transport by atmospheric rivers with related precipitation over sea ice, as well a distinct synoptic-scale Arctic storm event transporting pulses of heat and moisture into the Arctic have been observed in detail during this campaign. Cold air outbreaks are another facet of Arctic-mid-latitude linkages that have been probed during HALO–(\mathcal{AC})³. The following questions will be investigated in future studies: (i) How do cloud microphysical and radiative properties and vertical mixing affect air mass transformation and precipitation, and how are these processes represented in models of different resolution? (ii) What is the role of anomalous moisture transport into the Arctic for precipitation, and what are its impacts on the surface energy budget and ice-ocean conditions along its pathway?

6. Summary

Arctic amplification represents a major and alarming sign of currently ongoing climate changes. In 2016, the Transregional Collaborative Research Center (\mathcal{AC})³ was established to investigate atmospheric and surface processes and feedback mechanisms contributing to the phenomenon of Arctic amplification. Since then the project has successfully performed comprehensive observations and data analysis, in concert with extensive modeling activities on different temporal (long- and short-term campaigns, satellite observations over several decades) and spatial (from centimeter-scale turbulence to global circulation) scales. Some of the results achieved within (\mathcal{AC})³ since its beginning in 2016, are summarized in the following.

a. Trends of Arctic Amplification-relevant Parameters

Indications of trends of several climate-relevant parameters in the Arctic have been revealed, which shed new light on processes determining Arctic amplification. An obvious moistening of the central Arctic for all seasons with the highest absolute trend in summer (larger than 0.3 mm per decade) and lowest value in winter (less than 0.2 mm per decade) was detected (1979-2016). Over the Atlantic sector and large parts of the central Arctic Ocean, the moistening is most obvious in fall and winter. This trend has been linked with an increased occurrence and persistence of Arctic storms transporting moist warm air into the Arctic, causing an amplified winter warming in the Svalbard and North Pole regions. The increased moisture advection via the North Atlantic pathway has been attributed to an enhanced occurrence of the Scandinavia/Ural blocking in early winter. The mean annual sea ice thickness in Fram Strait decreased by 15 % per decade (1990–2014), as well as the Arctic sea ice volume export through the Fram Strait (27 % per decade, 1992-2014). For the time period of 2003-2020, a significant decrease of snow depth on sea ice in March of 12 % per decade for first-year ice was observed; for multi-year ice the decrease was smaller (9 % per decade). In addition, a positive tropospheric BrO trend of about 15 % per decade during polar spring was identified, correlated with the increase in first-year ice.

b. Enhanced Process Understanding

Surface albedo-cloud interactions were identified as an influential component in calculations of cloud radiative forcing. A four-mode structure of the surface radiative energy budget was revealed based on observations, and this structure was sufficiently reproduced by the ICON model. The presence of cloud layers above the dominant boundary layer clouds was found to significantly impact the lower cloud by damping cloud top cooling and turbulent fluxes. However, in general, clouds remain a major issue in models, on all scales. The quantitative impact of black carbon on radiative forcing in the Arctic during polar day still appears unclear. A seasonal variation of INP concentrations and indications for both, terrestrial and marine/biogenic INP sources have been found. Marine/biological particles within the upper ocean have been shown to significantly absorb solar radiation and thus to contribute to warming of the ocean mixed layer. The vertical atmospheric stability determines the coupling of the surface with cloud processes, while humidity may feed clouds from below and/or above. Air mass transformations during meridional transport

are poorly represented in models. To improve this situation, the recent HALO-(\mathcal{AC})³ airborne campaign has provided promising measurements (Wendisch et al. 2021).

c. Improved Parameterizations

The exploitation of observational data has led to improved parameterizations that have been implemented in various models. To improve the model representation of the surface albedo feedback, models have been equipped with new sea ice albedo parameterizations derived from field measurements, which also consider the dependence of surface albedo on cloud properties. Revised parameterizations of convective plumes and related processes over leads of different widths have been established. Turbulent energy flux parameterizations for very stable surface layers using Monin-Obukhov similarity theory stability functions have led to an improved reproduction of transfer coefficients in the very stable surface layer. Systematic comparisons of simulations with measurements have revealed further open issues in models. For example, the cloud droplet activation scheme of ICON was revised, scaling the default CCN profile, representative for a more polluted atmosphere, to be in better agreement with actually observed CCN concentrations and, furthermore, by using a representation of the turbulence impact on cloud-scale updraft speeds.

It is clear that these broad themes are all essential components of amplified Arctic change. In the coming years (\mathcal{AC})³ aims to understand how these work together to determine the degree of amplification and the future trajectory of the Arctic climate system.

Acknowledgments. We gratefully acknowledge the funding by the German Research Foundation (DFG, Deutsche Forschungsgemeinschaft) of the Transregional Collaborative Research Center SFB/TRR 172 (Project-ID 268020496), the Priority Programs SPP 1294 (HALO) and SPP 2115 (PROM). We thank AWI for financing most of the flight hours of Polar 5 and Polar 6 and extremely professional logistic support. Part of this work was carried out and data used in this manuscript was produced as part of MOSAiC with the tag MOSAiC20192020. We thank all persons involved in the expedition of the RV Polarstern during MOSAiC in 2019-2020 (AWI_PS122_00) as listed in Nixdorf et al. (2021). We are also grateful to the German Climate Computing Center (Deutsches Klimarechenzentrum, DKRZ) for the computing time and services provided, as well as to the German Weather Service (Deutscher Wetterdienst, DWD) for cooperation and support.

Data availability statement. All data gathered or created within the $(\mathcal{AC})^3$ project are subject to an agreed data policy (http://www.ac3-tr.de/wp-content/uploads/2020/11/ac3_data_policy_202008.pdf) and are already publicly accessible or will be made available. Currently, more than 1000 data sets from the $(\mathcal{AC})^3$ project can be downloaded freely via the PAN-GAEA data publisher (<http://data.ac3-tr.de> or <https://www.pangaea.de/?q=project:label:AC3>). An additional special *ac3airborne python package* (https://igmk.github.io/how_to_ac3airborne/intro.html) can be used to analyze data collected during the various airborne campaigns conducted within $(\mathcal{AC})^3$. Daily updated satellite sea ice data can be downloaded freely (<https://seaice.uni-bremen.de>). We invite the international scientific community working on Arctic climate topics to use the wealth of collected observational data and modeling results from $(\mathcal{AC})^3$ for joint analyses.

APPENDIX

List of acronyms (in alphabetic order).

ABL	Atmospheric Boundary Layer
(\mathcal{AC}) ³	Arctic Amplification: Climate Relevant Atmospheric and Surface Processes, and Feedback Mechanisms
ACLOUD	Arctic CLOUD Observations Using airborne measurements during polar Day
AFLUX	Airborne measurements of radiative and turbulent FLUXes in the cloudy atmospheric boundary layer
ALADINA	Application of Light-weight Aircraft for Detecting in-situ Aerosols
AWI	Alfred–Wegener–Institut, Helmholtz–Zentrum für Polar– und Meeresforschung
AWIPEV	Alfred Wegener Institute for Polar and Marine Research (AWI) and the French Polar Institute Paul Emile Victor (IPEV)
BC	Black Carbon
BELUGA	Balloon-bornE moduLar Utility for profilinG the lower Atmosphere
CCN	Cloud Condensation Nuclei
CDOM	Colored Dissolved Organic Matter
CER	Cloud Effective Radius
CMIP5	Coupled Model Intercomparison Project Phase 5
COT	Cloud Optical Thickness
FASMAR	Fast and Accurate Semi-analytical Model of Atmosphere-surface Reflectance)
FYI	First-Year Sea Ice
GCM	Global Circulation Model
HALO	High Altitude and Long Range Research Aircraft
HIRHAM	High-Resolution Limited Area Model
ICON	ICOsahedral Non-hydrostatic
INPs	Ice Nucleating Particles
IWP	Ice Water Path
IWV	Integrated Water Vapor
LEIPSIC	Light Estimator Including Polarization, Surface Inhomogeneities, and Clouds
LES	Large–Eddy Simulations
LWC	Liquid Water Content
LWP	Liquid Water Path

MERRA	NASA Modern Era Retrospective analysis for Research and Applications
MiRAC	Microwave Radar/radiometer for Arctic Clouds
MITgcm	Massachusetts Institute of Technology General Circulation Model
MIZ	Marginal Sea Ice Zone
MOSAiC	Multidisciplinary drifting Observatory for the Study of Arctic Climate
MOSAiC-ACA	Atmospheric Airborne observations in the Central Arctic
MOST	Monin-Obukhov Similarity Theory
MYI	Multi-Year Sea Ice
NAO	North Atlantic Oscillation
NAOSIM	North Atlantic/Arctic Ocean-Sea Ice Model
NDACC	Network for the Detection of Atmospheric Composition Change
PAMARCMiP	Polar Airborne Measurements and Arctic Regional Climate Model Simulation Project
PAMTRA	Passive and Active Microwave radiative TRAnsfer tool for simulating radiometer and radar measurements of the cloudy atmosphere
PASCAL	Physical feedback of Arctic ABL, Sea ice, Cloud and Aerosol
PG	Phytoplankton Groups
RRTMG	Rapid Radiative Transfer Model for GCMs
RV	Research Vessel
SCIATRAN	Radiative Transfer and Retrieval Algorithm
SFV	Stability Correction Function
SML	Sea Surface Microlayer
SHEBA	Surface Heat Budget of the Arctic Ocean
SWIFT	Fast ozone chemistry scheme for interactive calculation of the extrapolar stratospheric ozone layer in coupled general circulation models
TCCON	Total Carbon Column Observing Network
TSM	Total Suspended Matter

References

- Akperov, M., V. A. Semenov, I. I. Mokhov, W. Dorn, and A. Rinke, 2020: Impact of Atlantic water inflow on winter cyclone activity in the Barents Sea: Insights from coupled regional climate model simulations. *Environ. Res. Lett.*, **15** (2), 024009, <https://doi.org/10.1088/1748-9326/ab6399>.
- Ardyna, M., and K. Arrigo, 2020: Phytoplankton dynamics in a changing Arctic Ocean. *Nat. Clim. Change*, **10**, 892–903, <https://doi.org/10.1038/s41558-020-0905-y>.
- Armour, K. C., N. Siler, A. Donohoe, and G. H. Roe, 2019: Meridional atmospheric heat transport constrained by energetics and mediated by large-scale diffusion. *J. Clim.*, **32**, 3655–3680, <https://doi.org/10.1175/JCLI-D-18-0563.1>.
- Arrhenius, S., 1896: XXXI. On the influence of carbonic acid in the air upon the temperature of the ground. *The London, Edinburgh, and Dublin Philosophical Magazine and Journal of Science*, **41** (251), 237–276, <https://doi.org/10.1080/14786449608620846>.
- Barrientos-Velasco, C., H. Deneke, H. Griesche, P. Seifert, R. Engelmann, and A. Macke, 2020: Spatiotemporal variability of solar radiation introduced by clouds over Arctic sea ice. *Atmos. Meas. Tech.*, **13** (4), 1757–1775, <https://doi.org/10.5194/amt-13-1757-2020>.
- Barrientos-Velasco, C., H. Deneke, A. Hünnerbein, H. J. Griesche, P. Seifert, and A. Macke, 2022: Radiative closure and cloud effects on the radiation budget based on satellite and shipborne observations during the Arctic summer research cruise, PS106. *Atmos. Chem. Phys.*, **22**, 9313–9348, <https://doi.org/10.5194/acp-22-9313-2022>.
- Barthlott, S., and Coauthors, 2017: Tropospheric water vapour isotopologue data H_2^{16}O , H_2^{18}O , and HD^{16}O as obtained from NDACC/FTIR solar absorption spectra. *Earth Syst. Sci. Data*, **9** (1), 15–29, <https://doi.org/10.5194/essd-9-15-2017>.
- Baum, B., P. Yang, A. Heymsfield, C. Schmitt, Y. Xie, A. Bansemer, Y. Hu, and Z. Zhang, 2011: Improvements in shortwave bulk scattering and absorption models for the remote sensing of ice clouds. *J. Appl. Meteor. Climatol.*, **50**, 1037–1056, <https://doi.org/10.1175/2010JAMC2608.1>.

- Beljaars, A. C. M., and A. A. M. Holtslag, 1991: Flux parameterization over land surfaces for atmospheric models. *J. Appl. Meteorol.*, **30** (3), 327–341, [https://doi.org/10.1175/1520-0450\(1991\)030<0327:FPOLSF>2.0.CO;2](https://doi.org/10.1175/1520-0450(1991)030<0327:FPOLSF>2.0.CO;2).
- Blackport, R., and J. A. Screen, 2020: Insignificant effect of Arctic amplification on the amplitude of midlatitude atmospheric waves. *Science Advances*, **6** (8), eaay2880, <https://www.science.org/doi/abs/10.1126/sciadv.aay2880>.
- Block, K., F. Schneider, J. Mülmenstädt, M. Salzmann, and J. Quaas, 2020: Climate models disagree on the sign of total radiative feedback in the Arctic. *Tellus A*, **72:1**, 1–14, <https://doi.org/10.1080/16000870.2019.1696139>.
- Boeke, R. C., P. C. Taylor, and S. A. Sejas, 2021: On the nature of the Arctic’s positive lapse-rate feedback. *Geophys. Res. Lett.*, **48** (1), e2020GL091109, <https://doi.org/10.1029/2020GL091109>.
- Bougoudis, I., A.-M. Blechschmidt, A. Richter, S. Seo, J. P. Burrows, N. Theys, and A. Rinke, 2020: Long-term time series of Arctic tropospheric BrO derived from UV–VIS satellite remote sensing and its relation to first-year sea ice. *Atmos. Chem. Phys.*, **20** (20), 11 869–11 892, <https://doi.org/10.5194/acp-20-11869-2020>.
- Box, J. E., A. Wehrlé, D. van As, R. S. Fausto, K. K. Kjeldsen, A. Dachauer, A. P. Ahlstrøm, and G. Picard, 2022: Greenland ice sheet rainfall, heat and albedo feedback impacts from the mid-august 2021 atmospheric river. *Geophys. Res. Lett.*, **49** (11), e2021GL097356, <https://doi.org/10.1029/2021GL097356>.
- Bresson, H., and Coauthors, 2022: Case study of a moisture intrusion over the Arctic with the ICOSahedral Non-hydrostatic (ICON) model: Resolution dependence of its representation. *Atmos. Chem. Phys.*, **22** (1), 173–196, <https://doi.org/10.5194/acp-22-173-2022/>.
- Budyko, M. I., 1969: The effect of solar radiation variations on the climate of the Earth. *Tellus*, **21**, 611–619, <https://doi.org/10.1111/j.2153--3490.1969.tb00466.x>.
- Buschmann, M., N. M. Deutscher, M. Palm, T. Warneke, C. Weinzierl, and J. Notholt, 2017: The Arctic seasonal cycle of total column CO₂ and CH₄ from ground-based solar and lunar

- FTIR absorption spectrometry. *Atmos. Meas. Tech.*, **10** (7), 2397–2411, <https://doi.org/10.5194/amt-10-2397-2017>.
- Businger, J. A., J. C. Wyngaard, Y. Izumi, and E. F. Bradley, 1971: Flux-profile relationships in the atmospheric surface layer. *J. Atmos. Sci.*, **28** (2), 181–189, [https://doi.org/10.1175/1520-0469\(1971\)028<0181:FPRITA>2.0.CO;2](https://doi.org/10.1175/1520-0469(1971)028<0181:FPRITA>2.0.CO;2).
- Chechin, D. G., C. Lüpkes, J. Hartmann, A. Ehrlich, and M. Wendisch, 2022: Turbulent structure of the Arctic boundary layer in early summer driven by stability, wind shear and cloud top radiative cooling: ACLOUD airborne observations. *Atmos. Chem. Phys. Discuss. [preprint]*, **in review**, 1–42, <https://acp.copernicus.org/preprints/acp-2022-398/>.
- Chechin, D. G., I. A. Makhotina, C. Lüpkes, and A. P. Makshtas, 2019: Effect of wind speed and leads on clear-sky cooling over Arctic sea ice during polar night. *J. Atmos. Sci.*, **76** (8), 2481–2503, <https://doi.org/10.1175/JAS-D-18-0277.1>.
- Chylik, J., D. Chechin, R. Dupuy, B. S. Kulla, C. Lüpkes, S. Mertes, M. Mech, and R. A. J. Neggers, 2021: Aerosol-cloud-turbulence interactions in well-coupled Arctic boundary layers over open water. *Atmos. Chem. Phys. Discuss.*, 1–42, <https://doi.org/10.5194/acp-2021-888>, in review.
- Cohen, J., and Coauthors, 2014: Recent Arctic amplification and extreme mid-latitude weather. *Nat. Geosci.*, **7**, 627–637, <https://doi.org/10.1038/ngeo2234>.
- Cohen, J., and Coauthors, 2020: Divergent consensus on Arctic amplification influence on midlatitude severe winter weather. *Nat. Clim. Change*, **10**, 20–29, <https://doi.org/10.1038/s41558-019-0662-y>.
- Crasemann, B., D. Handorf, R. Jaiser, K. Dethloff, T. Nakamura, J. Ukita, and K. Yamazaki, 2017: Can preferred atmospheric circulation patterns over the North-Atlantic-Eurasian region be associated with Arctic sea ice loss? *Polar Sci.*, **14**, 9–20, <https://doi.org/10.1016/j.polar.2017.09.002>.
- Crawford, A. D., J. V. Lukovich, M. R. McCrystall, J. C. Stroeve, and D. G. Barber, 2022: Reduced sea ice enhances intensification of winter storms over the Arctic Ocean. *J. Clim.*, **35** (11), 3353 – 3370, <https://doi.org/10.1175/JCLI-D-21-0747.1>.

- Crewell, S., and Coauthors, 2021: A systematic assessment of water vapor products in the Arctic: From instantaneous measurements to monthly means. *Atmos. Meas. Tech.*, **14** (7), 4829–4856, <https://doi.org/10.5194/amt-14-4829-2021>.
- Dahlke, S., and M. Maturilli, 2017: Contribution of atmospheric advection to the amplified winter warming in the Arctic North Atlantic region. *Adv. Meteorol.*, <https://doi.org/10.1155/2017/4928620>.
- Donth, T., E. Jäkel, A. Ehrlich, B. Heinold, J. Schacht, A. Herber, M. Zanatta, and M. Wendisch, 2020: Combining atmospheric and snow radiative transfer models to assess the solar radiative effects of black carbon in the Arctic. *Atmos. Chem. Phys.*, **20** (13), 8139–8156, <https://doi.org/10.5194/acp-20-8139-2020>.
- Dorn, W., A. Rinke, C. Köberle, K. Dethloff, and R. Gerdes, 2019: Evaluation of the sea-ice simulation in the upgraded version of the coupled regional atmosphere-ocean-sea ice model HIRHAM–NAOSIM 2.0. *Atmosphere*, **10** (8), <https://doi.org/10.3390/atmos10080431>.
- Dyer, A., 1974: A review of flux-profile relationships. *Boundary-Layer Meteorol.*, **7** (3), 363–372.
- Ebell, K., T. Nomokonova, M. Maturilli, and C. Ritter, 2020: Radiative effect of clouds at Ny–Ålesund, Svalbard, as inferred from ground-based remote sensing observations. *J. Appl. Meteor. Climatol.*, **59**(1), 3–22, <https://doi.org/10.1175/JAMC-D-19-0080.1>.
- Egerer, U., A. Ehrlich, M. Gottschalk, H. Griesche, R. A. J. Neggers, H. Siebert, and M. Wendisch, 2021: Case study of a humidity layer above Arctic stratocumulus and potential turbulent coupling with the cloud top. *Atmos. Chem. Phys.*, **21** (8), 6347–6364, <https://doi.org/10.5194/acp-21-6347-2021>.
- Egerer, U., M. Gottschalk, H. Siebert, A. Ehrlich, and M. Wendisch, 2019: A new setup for combined turbulence and radiation measurements using a tethered balloon in the cloudy Arctic. *Atmos. Meas. Tech.*, **12** (7), 4019–4038, <https://doi.org/10.5194/amt-12-4019-2019>.
- Ehrlich, A., and Coauthors, 2019: A comprehensive in situ and remote sensing data set from the Arctic CLOUD Observations Using airborne measurements during polar Day (ACLOUD) campaign. *Earth Syst. Sci. Data*, **11** (4), 1853–1881, <https://doi.org/10.5194/essd-11-1853-2019>.

- Engelmann, R., and Coauthors, 2021: Wildfire smoke, Arctic haze, and aerosol effects on mixed-phase and cirrus clouds over the North Pole region during MOSAiC: An introduction. *Atmos. Chem. Phys.*, **21** (17), 13 397–13 423, <https://doi.org/10.5194/acp-21-13397-2021>.
- Flanner, M. G., 2013: Arctic climate sensitivity to local black carbon. *J. Geophys. Res. Atmos.*, **118** (4), 1840–1851, <https://doi.org/10.1002/jgrd.50176>.
- Francis, J. A., and S. J. Vavrus, 2015: Evidence for a wavier jet stream in response to rapid Arctic warming. *Environ. Res. Lett.*, **10** (1), 014 005, <https://doi.org/10.1088/1748-9326/10/1/014005>.
- Gierens, R., S. Kneifel, M. D. Shupe, K. Ebell, M. Maturilli, and U. Löhnert, 2020: Low-level mixed-phase clouds in a complex Arctic environment. *Atmos. Chem. Phys.*, **20** (6), 3459–3481, <https://doi.org/10.5194/acp-20-3459-2020>.
- Gliß, J., and Coauthors, 2021: AeroCom phase III multi-model evaluation of the aerosol life cycle and optical properties using ground- and space-based remote sensing as well as surface in situ observations. *Atmos. Chem. Phys.*, **21** (1), 87–128, <https://acp.copernicus.org/articles/21/87/2021/>.
- Goosse, H., and Coauthors, 2018: Quantifying climate feedbacks in polar regions. *Nature Comm.*, **9**, 1919, <https://doi.org/10.1038/s41467-018-04173-0>.
- Gorodetskaya, I., T. Silva, H. Schmithüsen, and N. Hirasawa, 2020: Atmospheric river signatures in radiosonde profiles and reanalyses at the Dronning Maud Land Coast, East Antarctica. *Adv. Atmos. Sci.*, **37** (AAS-2019-0221), 455, <https://doi.org/10.1007/s00376-020-9221-8>.
- Grachev, A. A., E. L. Andreas, C. W. Fairall, P. S. Guest, and P. O. G. Persson, 2007: SHEBA flux–profile relationships in the stable atmospheric boundary layer. *Boundary-Layer Meteorol.*, **124** (3), 315–333, <https://doi.org/10.1007/s10546-007-9177-6>.
- Graham, R. M., L. Cohen, A. A. Petty, L. N. Boisvert, A. Rinke, S. R. Hudson, M. Nicolaus, and M. A. Granskog, 2017a: Increasing frequency and duration of Arctic winter warming events. *Geophys. Res. Lett.*, **44**, 6974–698, <https://doi.org/10.1002/2017GL073395>.
- Graham, R. M., and Coauthors, 2017b: A comparison of the two Arctic atmospheric winter states observed during N-ICE2015 and SHEBA. *J. Geophys. Res. Atmos.*, **122** (11), 5716–5737, <https://doi.org/10.1002/2017GL073395>.

- Griesche, H. J., K. Ohneiser, P. Seifert, M. Radenz, R. Engelmann, and A. Ansmann, 2021: Contrasting ice formation in Arctic clouds: Surface-coupled vs. surface-decoupled clouds. *Atmos. Chem. Phys.*, **21** (13), 10 357–10 374, <https://doi.org/10.5194/acp-21-10357-2021>.
- Griesche, H. J., and Coauthors, 2020: Application of the shipborne remote sensing supersite OCEANET for profiling of Arctic aerosols and clouds during *Polarstern* cruise PS106. *Atmos. Meas. Tech.*, **13** (10), 5335–5358, <https://doi.org/10.5194/amt-13-5335-2020>.
- Gryanik, V. M., and C. Lüpkes, 2018: An efficient non-iterative bulk parametrization of surface fluxes for stable atmospheric conditions over polar sea-ice. *Boundary-Layer Meteorol.*, **166**, 301–325, <https://doi.org/10.1007/s10546-017-0302-x>.
- Gryanik, V. M., and C. Lüpkes, 2022: A package of momentum and heat transfer coefficients for the stable surface layer extended by new coefficients over sea ice. *Boundary-Layer Meteorol.*, **accepted**.
- Gryanik, V. M., C. Lüpkes, A. Grachev, and D. Sidorenko, 2020: New modified and extended stability functions for the stable boundary layer based on SHEBA and parametrizations of bulk transfer coefficients for climate models. *J. Atmos. Sci.*, <https://doi.org/10.1175/JAS-D-19-0255.1>.
- Gryanik, V. M., C. Lüpkes, D. Sidorenko, and A. Grachev, 2021: A universal approach for the non-iterative parametrization of near-surface turbulent fluxes in climate and weather prediction models. *J. Adv. Model. Earth Syst.*, **13** (8), e2021MS002 590, <https://doi.org/10.1029/2021MS002590>.
- Guan, B., and D. E. Waliser, 2019: Tracking atmospheric rivers globally: Spatial distributions and temporal evolution of life cycle characteristics. *J. Geophys. Res. Atmos.*, **124** (23), 12 523–12 552, <https://doi.org/10.1029/2019JD031205>.
- Hall, A., 2004: The role of surface albedo feedback in climate. *J. Clim.*, **17**, 1550–1568, [https://doi.org/10.1175/1520-0442\(2004\)017<1550:TROSAF>2.0.CO;2](https://doi.org/10.1175/1520-0442(2004)017<1550:TROSAF>2.0.CO;2).
- Hartmann, M., T. Blunier, S. O. Brügger, J. Schmale, M. Schwikowski, A. Vogel, H. Wex, and F. Stratmann, 2019: Variation of ice nucleating particles in the European Arctic over the last centuries. *Geophys. Res. Lett.*, **46** (7), 4007–4016, <https://doi.org/10.1029/2019GL082311>.

- Hartmann, M., and Coauthors, 2020: Wintertime airborne measurements of ice nucleating particles in the high Arctic: A hint to a marine, biogenic source for ice nucleating particles. *Geophys. Res. Lett.*, **47** (13), e2020GL087770, <https://doi.org/10.1029/2020GL087770>.
- Hartmann, M., and Coauthors, 2021: Terrestrial or marine – indications towards the origin of ice-nucleating particles during melt season in the European Arctic up to 83.7° N. *Atmos. Chem. Phys.*, **21** (15), 11 613–11 636, <https://doi.org/10.1029/2020GL087770>.
- Hofmann, Z., W.-J. von Appen, and C. Wekerle, 2021: Seasonal and mesoscale variability of the two Atlantic water recirculation pathways in Fram Strait. *J. Geophys. Res. Oceans*, **126** (7), e2020JC017057, <https://doi.org/10.1029/2020JC017057>.
- Huang, Y., and Coauthors, 2019: Thicker clouds and accelerated Arctic sea ice decline: The atmosphere-sea ice interactions in spring. *Geophys. Res. Lett.*, **46** (12), 6980–6989, <https://doi.org/10.1029/2019GL082791>.
- Inoue, J., and Coauthors, 2021: Clouds and radiation processes in regional climate models evaluated using observations over the ice-free Arctic Ocean. *J. Geophys. Res. Atmos.*, **126** (1), e2020JD033904, <https://doi.org/10.1029/2020JD033904>.
- Jafariserajehlou, S., L. Mei, M. Vountas, V. Rozanov, J. Philip Burrows, and R. Hollmann, 2019: A cloud identification algorithm over the Arctic for use with AATSR/SLSTR measurements. *Atmos. Meas. Tech.*, **12**(2), 1059–1076, <https://doi.org/10.5194/amt-2018-231>.
- Jaiser, R., T. Nakamura, D. Handorf, K. Dethloff, J. Ukita, and K. Yamazaki, 2016: Atmospheric winter response to Arctic sea ice changes in reanalysis data and model simulations. *J. Geophys. Res.*, **121** (13), 7564–7577, <https://doi.org/10.1002/2015JD024679>.
- Jäkel, E., J. Stapf, M. Wendisch, M. Nicolaus, W. Dorn, and A. Rinke, 2019: Validation of the sea ice surface albedo scheme of the regional climate model HIRHAM–NAOSIM using aircraft measurements during the ACLOUD/PASCAL campaigns. *Cryosphere*, **13**, 1695–1708, <https://doi.org/10.5194/tc-13-1695-2019>.
- Jeffries, M. O., J. E. E. Overland, and D. K. Perovich, 2013: The Arctic shifts to a new normal. *Phys. Today*, **66**, 35–40, <https://doi.org/10.1063/PT.3.2147>.

- Kay, J. E., and A. Gettelman, 2009: Cloud influence on and response to seasonal Arctic sea ice loss. *J. Geophys. Res. Atmos.*, **114**, D18 204, <https://doi.org/10.1029/2009JD011773>.
- Kecorius, S., and Coauthors, 2019: New particle formation and its effect on cloud condensation nuclei abundance in the summer Arctic: A case study in the Fram Strait and Barents Sea. *Atmos. Chem. Phys.*, **19** (22), 14 339–14 364, <https://doi.org/10.5194/acp-19-14339-2019>.
- Kodros, J. K., and Coauthors, 2018: Size-resolved mixing state of black carbon in the Canadian high Arctic and implications for simulated direct radiative effect. *Atmos. Chem. Phys.*, **18**, 11 345–11 361, <https://doi.org/10.5194/acp-18-11345-2018>.
- Kovács, T., R. Gerdes, and J. Marshall, 2020: Wind feedback mediated by sea ice in the Nordic Seas. *J. Climate*, **33** (15), 6621–6632, <https://doi.org/10.1175/JCLI-D-19-0632.1>.
- Kretzschmar, J., M. Salzmann, J. Mülmenstädt, and J. Quaas, 2019: Arctic clouds in ECHAM6 and their sensitivity to cloud microphysics and surface fluxes. *Atmos. Chem. Phys.*, **19** (16), 10 571–10 589, <https://doi.org/10.5194/acp-19-10571-2019>.
- Kretzschmar, J., J. Stapf, D. Klocke, M. Wendisch, and J. Quaas, 2020: Employing airborne radiation and cloud microphysics observations to improve cloud representation in ICON at kilometer-scale resolution in the Arctic. *Atmos. Chem. Phys.*, **20** (21), 13 145–13 165, <https://doi.org/10.5194/acp-20-13145-2020>.
- Kruppen, T., and Coauthors, 2021: MOSAiC drift expedition from October 2019 to July 2020: sea ice conditions from space and comparison with previous years. *Cryosphere*, **15** (8), 3897–3920, <https://doi.org/10.5194/tc-15-3897-2021>.
- Kulla, B. S., and C. Ritter, 2019: Water vapor calibration: Using a Raman lidar and radiosoundings to obtain highly resolved water vapor profiles. *Remote Sens.*, **11** (6), <https://doi.org/10.3390/rs11060616>.
- Lampert, A., and Coauthors, 2020: Unmanned aerial systems for investigating the polar atmospheric boundary layer—technical challenges and examples of applications. *Atmosphere*, **11** (4), <https://doi.org/10.3390/atmos11040416>.

- Lauer, M., K. Block, M. Salzmänn, and J. Quaas, 2020: CO₂-forced changes of Arctic temperature lapse rates in CMIP5 models. *Meteorol. Z.*, **29** (1), 79–93, <https://doi.org/10.1127/metz/2020/0975>.
- Lelli, L., M. Vountas, N. Khosravi, and J. P. Burrows, 2022: Satellite-based evidence of regional and seasonal Arctic cooling by brighter and wetter clouds. *Atmos. Chem. Phys. Discuss.*, in review, <https://doi.org/10.5194/acp-2022-28>.
- Linke, O., and J. Quaas, 2022: The impact of CO₂-driven climate change on the Arctic atmospheric energy budget in CMIP6 climate model simulations. *Tellus A*, **74**, 106–118, <http://doi.org/10.16993/tellusa.29>.
- Loewe, K., A. M. L. Ekman, M. Paukert, J. Sedlar, M. Tjernström, and C. Hoose, 2017: Modelling micro- and macrophysical contributors to the dissipation of an arctic mixed-phase cloud during the arctic summer cloud ocean study (ascos). *Atmos. Chem. Phys.*, **17** (11), 6693–6704, <https://doi.org/10.5194/acp-17-6693-2017>.
- Lonardi, M., and Coauthors, 2022: Tethered balloon-borne profile measurements of atmospheric properties in cloudy conditions over Arctic sea-ice during MOSAiC: Overview and first results. *Elem. Sci. Anth.*, accepted.
- Losa, S., and Coauthors, 2017: Synergistic exploitation of hyper- and multispectral precursor Sentinel measurements to determine Phytoplankton Functional Types (SynSenPFT). *Front. Mar. Sci.*, **4**: 203, <https://doi.org/10.3389/fmars.2017.00203>.
- Louis, J.-F., 1979: A parametric model of vertical eddy fluxes in the atmosphere. *Boundary-Layer Meteorol.*, **17** (2), 187–202.
- Lu, J., G. Heygster, and G. Spreen, 2018: Atmospheric correction of sea ice concentration retrieval for 89 GHz AMSR-E observations. *IEEE J-STARS*, **11** (5), 1442–1457, <https://doi.org/10.1109/jstars.2018.2805193>.
- Lu, J., G. Heygster, G. Spreen, and R. Scarlat, 2022: Reducing weather influences on sea ice concentration retrieval at 89 GHz using passive microwave observations. *J. Geophys. Res. Oceans*, in review.

- Ludwig, V., G. Spreen, and L. T. Pedersen, 2020: Evaluation of a new merged sea-ice concentration dataset at 1 km resolution from thermal infrared and passive microwave satellite data in the Arctic. *Remote Sens.*, **12** (19), <https://doi.org/10.3390/rs12193183>.
- Lund, M. T., B. H. Samset, R. B. Skeie, D. Watson-Parris, J. M. Katich, J. P. Schwarz, and B. Weinzierl, 2018: Short black carbon lifetime inferred from a global set of aircraft observations. *npj Clim. Atmos. Sci.*, **31**, 1–8, <https://doi.org/10.1038/s41612-018-0040-x>.
- Lüpkes, C., T. Vihma, G. Birnbaum, and U. Wacker, 2008: Influence of leads in sea ice on the temperature of the atmospheric boundary layer during polar night. *Geophys. Res. Lett.*, **35** (3), <https://doi.org/10.1029/2007gl032461>.
- Manabe, S., and R. T. Wetherald, 1975: The effects of doubling the CO₂ concentration on the climate of a general circulation model. *J. Atmos. Sci.*, **32**, 3–15, [https://doi.org/10.1175/1520-0469\(1975\)032<0003:TEODTC>2.0.CO;2](https://doi.org/10.1175/1520-0469(1975)032<0003:TEODTC>2.0.CO;2).
- Markus, T., and Coauthors, 2006: Microwave signatures of snow on sea ice: Observations. *IEEE Trans. Geosci. Remote Sens.*, **44** (11), 3081–3090, <https://doi.org/10.1109/TGRS.2006.883134>.
- McCrystall, M. R., J. Stroeve, M. Serreze, B. C. Forbes, and J. A. Screen, 2021: New climate models reveal faster and larger increases in Arctic precipitation than previously projected. *Nat. Commun.*, **12**, 6765, <https://doi.org/10.1038/s41467-021-27031-y>.
- Mech, M., L.-L. Kliesch, A. Anhäuser, T. Rose, P. Kollias, and S. Crewell, 2019: Microwave Radar/radiometer for Arctic Clouds (MiRAC): First insights from the ACLOUD campaign. *Atmos. Meas. Tech.*, **12** (9), 5019–5037, <https://doi.org/10.5194/amt-12-5019-2019>.
- Mech, M., M. Maahn, S. Kneifel, D. Ori, E. Orlandi, P. Kollias, V. Schemann, and S. Crewell, 2020: PAMTRA 1.0: the Passive and Active Microwave radiative TRAnsfer tool for simulating radiometer and radar measurements of the cloudy atmosphere. *Geosci. Model Dev.*, **13** (9), 4229–4251, <https://doi.org/10.5194/gmd-13-4229-2020>.
- Mech, M., and Coauthors, 2022: MOSAiC-ACA and AFLUX: Arctic airborne campaigns characterizing the exit area of MOSAiC. *Nature Scientific Data*, for submission.

- Mei, L., V. Rozanov, and J. P. Burrows, 2020a: A fast and accurate radiative transfer model for aerosol remote sensing. *J. Quant. Spectrosc. Radiat. Transfer*, **256**, 107 270, <https://doi.org/10.1016/j.jqsrt.2020.107270>.
- Mei, L., V. Rozanov, E. Jäkel, X. Cheng, M. Vountas, and J. P. Burrows, 2021a: The retrieval of snow properties from SLSTR Sentinel-3 – Part 2: Results and validation. *Cryosphere*, **15** (6), 2781–2802, <https://doi.org/10.5194/tc-15-2781-2021>.
- Mei, L., V. Rozanov, C. Pohl, M. Vountas, and J. P. Burrows, 2021b: The retrieval of snow properties from SLSTR Sentinel-3 – Part 1: Method description and sensitivity study. *Cryosphere*, **15** (6), 2757–2780, <https://doi.org/10.5194/tc-15-2757-2021>.
- Mei, L., V. Rozanov, C. Ritter, B. Heinold, Z. Jiao, M. Vountas, and J. P. Burrows, 2020b: Retrieval of aerosol optical thickness in the Arctic snow-covered regions using passive remote sensing: Impact of aerosol typing and surface reflection model. *IEEE Trans. Geosci. Remote Sens.*, 1–15, <https://doi.org/10.1109/TGRS.2020.2972339>.
- Mei, L., V. Rozanov, M. Vountas, and J. P. Burrows, 2018: The retrieval of ice cloud parameters from multi-spectral satellite observations of reflectance using a modified XBAER algorithm. *Remote Sens. Environ.*, **215**, 128–144, <https://doi.org/10.1016/j.rse.2018.06.007>.
- Mei, L., V. V. Rozanov, Z. Jiao, and J. P. Burrows, 2022: A new snow bidirectional reflectance distribution function model in spectral regions from UV to SWIR: Model development and application to ground-based, aircraft and satellite observation. *ISPRS Journal of Photogrammetry and Remote Sensing*, **188**, 269 –285, <https://doi.org/10.1016/j.isprsjprs.2022.04.010>.
- Mei, L., S. Vandenbussche, V. Rozanov, E. Proestakis, V. Amiridis, S. Callewaert, M. Vountas, and J. P. Burrows, 2020c: On the retrieval of aerosol optical depth over cryosphere using passive remote sensing. *Remote Sens. Environ.*, **241**, 111 731, <https://doi.org/10.1016/j.rse.2020.111731>.
- Metzner, E. P., M. Salzmänn, and R. Gerdes, 2020: Arctic Ocean surface energy flux and the cold halocline in future climate projections. *J. Geophys. Res. Oceans*, **125** (2), e2019JC015 554, <https://doi.org/10.1029/2019JC015554>.

- Mewes, D., and C. Jacobi, 2019: Heat transport pathways into the Arctic and their connections to surface air temperatures. *Atmos. Chem. Phys.*, **19** (6), 3927–3937, <https://doi.org/10.5194/acp-19-3927-2019>.
- Mewes, D., and C. Jacobi, 2020: Horizontal temperature fluxes in the Arctic in CMIP5 model results analyzed with self-organizing maps. *Atmosphere*, **11** (3), <https://doi.org/10.3390/atmos11030251>.
- Michaelis, J., and C. Lüpkes, 2022: The impact of lead patterns on mean profiles of wind, temperature, and turbulent fluxes in the atmospheric boundary layer over sea ice. *Atmosphere*, **13** (1), 148, <https://doi.org/10.3390/atmos13010148>.
- Michaelis, J., C. Lüpkes, A. U. Schmitt, and J. Hartmann, 2021: Modelling and parametrization of the convective flow over leads in sea ice and comparison with airborne observations. *Quart. J. Roy. Meteor. Soc.*, **147** (735), 914–943, <https://doi.org/10.1002/qj.3953>.
- Michaelis, J., C. Lüpkes, X. Zhou, M. Gryschka, and V. M. Gryanik, 2020: Influence of lead width on the turbulent flow over sea ice leads: Modeling and parametrization. *J. Geophys. Res. Atmos.*, **125**, e2019JD031996, <https://doi.org/10.1029/2019JD031996>.
- Mioche, G., and Coauthors, 2017: Vertical distribution of microphysical properties of Arctic springtime low-level mixed-phase clouds over the Greenland and Norwegian seas. *Atmos. Chem. Phys.*, **17** (20), 12 845–12 869, <https://doi.org/10.5194/acp-17-12845-2017>.
- Moon, T. A., M. L. Druckenmiller, and R. L. Thoman, 2021: Arctic Report Card 2021. <https://doi.org/10.25923/5s0f-5163>.
- Morrison, H., G. de Boer, G. Feingold, J. Harrington, M. D. Shupe, and K. Sulia, 2012: Resilience of persistent Arctic mixed-phase clouds. *Nat. Geosci.*, **5**, 11–17, <https://doi.org/10.1038/NGEO1332>.
- Naakka, T., T. Nygård, and T. Vihma, 2018: Arctic humidity inversions: Climatology and processes. *J. Climate*, **31**, 3765–3787, <https://doi.org/10.1175/JCLI-D-17-0497.1>.
- Nakoudi, K., C. Ritter, and I. S. Stachlewska, 2021a: Properties of cirrus clouds over the European Arctic (Ny-Ålesund, Svalbard). *Rem. Sens.*, **13** (22), <https://doi.org/10.3390/rs13224555>.

- Nakoudi, K., I. S. Stachlewska, and C. Ritter, 2021b: An extended lidar-based cirrus cloud retrieval scheme: First application over an Arctic site. *Opt. Express*, **29** (6), 8553–8580, <https://doi.org/10.1364/OE.414770>.
- Nakoudi, K., and Coauthors, 2020: Does the intra-Arctic modification of long-range transported aerosol affect the local radiative budget? (A case study). *Remote Sens.*, **12** (13), <https://doi.org/10.3390/rs12132112>.
- Nash, D., D. Waliser, B. Guan, H. Ye, and F. M. Ralph, 2018: The role of atmospheric rivers in extratropical and polar hydroclimate. *J. Geophys. Res. Atmos.*, **123** (13), 6804–6821, <https://doi.org/10.1029/2017JD028130>.
- Neff, W., 2018: Atmospheric rivers melt Greenland. *Nat. Clim. Change*, **8** (10), 857–858, <https://doi.org/10.1038/s41558-018-0297-4>.
- Neggers, R. A. J., J. Chylík, U. Egerer, H. Griesche, V. Schemann, P. Seifert, H. Siebert, and A. Macke, 2019: Local and remote controls on Arctic mixed-layer evolution. *J. Adv. Model. Earth Syst.*, **11**, 2214–2237, <https://doi.org/10.1029/2019MS001671>.
- Nicolaus, M., and Coauthors, 2022: Overview of the MOSAiC expedition: Snow and sea ice. *Elem. Sci. Anth.*, **10** (1), <https://doi.org/10.1525/elementa.2021.000046>.
- Nixdorf, U., and Coauthors, 2021: MOSAiC Extended Acknowledgement. <https://doi.org/10.5281/zenodo.5179739>.
- Nomokonova, T., K. Ebell, U. Löhnert, M. Maturilli, and C. Ritter, 2020: The influence of water vapor anomalies on clouds and their radiative effect at Ny-Ålesund. *Atmos. Chem. Phys.*, **20** (8), 5157–5173, <https://doi.org/10.5194/acp-20-5157-2020>.
- Nomokonova, T., K. Ebell, U. Löhnert, M. Maturilli, C. Ritter, and E. O’Connor, 2019: Statistics on clouds and their relation to thermodynamic conditions at Ny-Ålesund using ground-based sensor synergy. *Atmos. Chem. Phys.*, **19**, 1–22, <https://doi.org/10.5194/acp-19-1-2019>.
- Ohata, S., and Coauthors, 2021: Arctic black carbon during PAMARCMiP 2018 and previous aircraft experiments in spring. *Atmos. Chem. Phys.*, **21** (20), 15 861–15 881, <https://doi.org/10.5194/acp-21-15861-2021>.

- Ohneiser, K., and Coauthors, 2021: The unexpected smoke layer in the High Arctic winter stratosphere during MOSAiC 2019–2020. *Atmos. Chem. Phys.*, **21** (20), 15 783–15 808, <https://doi.org/10.5194/acp-21-15783-2021>.
- Olonscheck, D., T. Mauritsen, and D. Notz, 2019: Arctic sea-ice variability is primarily driven by atmospheric temperature fluctuations. *Nat. Geosci.*, **12**, 430–434, <https://doi.org/10.1038/s41561-019-0363-1>.
- Overland, J. E., K. R. Wood, and M. Wang, 2011: Warm Arctic–cold conditions: Impacts of the newly open Arctic Sea. *Polar Res.*, **30**, 15,787, <https://doi.org/10.3402/polar.v30i0.15787>.
- Pařilea, C., G. Heygster, M. Huntemann, and G. Spreen, 2019: Combined SMAP–SMOS thin sea ice thickness retrieval. *Cryosphere*, **13** (2), 675–691, <https://doi.org/10.5194/tc-13-675-2019>.
- Pefanis, V., S. N. Losa, M. Losch, M. A. Janout, and A. Bracher, 2020: Amplified Arctic surface warming and sea ice loss due to phytoplankton and colored dissolved material. *Geophys. Res. Lett.*, **47** (21), e2020GL088 795, <https://doi.org/10.1029/2020GL088795>.
- Pithan, F., and T. Mauritsen, 2014: Arctic amplification dominated by temperature feedbacks in contemporary climate models. *Nat. Geosci.*, **7**, 181–184, <https://doi.org/10.1038/ngeo2071>.
- Pithan, F., B. Medeiros, and T. Mauritsen, 2014: Mixed-phase clouds cause climate model biases in Arctic wintertime temperature inversions. *Clim. Dyn.*, **43** (1-2), 289–303, <https://doi.org/10.1007/s00382-013-1964-9>.
- Pithan, F., and Coauthors, 2018: Role of air-mass transformations in exchange between the Arctic and mid-latitudes. *Nat. Geosci.*, **11**, 805–812, <https://doi.org/10.1038/s41561-018-0234-1>.
- Pohl, C., L. Istomina, S. Tietsche, E. Jäkel, J. Stapf, G. Spreen, and G. Heygster, 2020: Broadband albedo of Arctic sea ice from MERIS optical data. *Cryosphere*, **14** (1), 165–182, <https://doi.org/10.5194/tc-14-165-2020>.
- Polyakov, I. V., and Coauthors, 2017: Greater role for Atlantic inflows on sea-ice loss in the Eurasian Basin of the Arctic Ocean. *Science*, **356**, 285–291, <https://doi.org/10.1126/science.aai8204>.

- Previdi, M., K. L. Smith, and L. M. Polvani, 2021: Arctic amplification of climate change: A review of underlying mechanisms. *Environ. Res. Lett.*, **16** (9), 093 003, <https://doi.org/10.1088/1748-9326/ac1c29>.
- Rabe, B., and Coauthors, 2022: Overview of the MOSAiC expedition: Physical oceanography. *Elem. Sci. Anth.*, **10** (1), <https://doi.org/10.1525/elementa.2021.00062>.
- Radovan, A., S. Crewell, E. M. Knudsen, and A. Rinke, 2019: Environmental conditions for polar low formation and development over the Nordic Seas: study of January cases based on the Arctic system reanalysis. *Tellus A*, **71** (1), 1618 131, <https://doi.org/10.1080/16000870.2019.1618131>.
- Rinke, A., E. Knudsen, D. Mewes, W. Dorn, D. Handorf, K. Dethloff, and J. C. Moore, 2019a: Arctic summer sea-ice melt and related atmospheric conditions in coupled regional climate model simulations and observations. *J. Geophys. Res.*, **124** (12), 6027–6039, <https://doi.org/10.1029/2018JD030207>.
- Rinke, A., M. Maturilli, R. M. Graham, H. Matthes, D. Handorf, L. Cohen, S. R. Hudson, and J. C. Moore, 2017: Extreme cyclone events in the Arctic: Wintertime variability and trends. *Environ. Res. Lett.*, **12** (9), <https://doi.org/10.1088/1748-9326/aa7def>.
- Rinke, A., and Coauthors, 2019b: Trends of vertically integrated water vapor over the Arctic during 1979–2016: Consistent moistening all over? *J. Climate*, **32** (18), 6097 – 6116, <https://doi.org/10.1175/JCLI-D-19-0092.1>.
- Ritter, C., and Coauthors, 2018: Microphysical properties and radiative impact of an intense biomass burning aerosol event measured over Ny-Ålesund, Spitsbergen in July 2015. *Tellus B*, **70** (1), 1–23, <https://doi.org/10.1080/16000889.2018.1539618>.
- Romanowsky, E., and Coauthors, 2019: The role of stratospheric ozone for Arctic-midlatitude linkages. *Sci. Rep.*, **9**, 7962, <https://doi.org/10.1038/s41598-019-43823-1>.
- Rostosky, P., G. Spreen, S. L. Farrell, T. Frost, G. Heygster, and C. Melsheimer, 2018: Snow depth retrieval on Arctic sea ice from passive microwave radiometers-improvements and extensions to multiyear ice using lower frequencies. *J. Geophys. Res. Oceans*, <https://doi.org/10.1029/2018jc014028>.

- Rostosky, P., G. Spreen, S. Gerland, M. Huntemann, and M. Mech, 2020: Modeling the microwave emission of snow on Arctic sea ice for estimating the uncertainty of satellite retrievals. *J. Geophys. Res. Oceans*, **125** (3), e2019JC015 465, <https://doi.org/10.1029/2019JC015465>.
- Rozanov, V. V., T. Dinter, A. V. Rozanov, A. Wolanin, A. Bracher, and P. Burrows J., 2017: Radiative transfer modeling through terrestrial atmosphere and ocean accounting for inelastic scattering processes: Software package SCIATRAN. *J. Quant. Spectrosc. Radiat. Transfer*, **194**, 65–85, <https://doi.org/10.1016/j.jqsrt.2017.03.009>.
- Ruiz-Donoso, E., and Coauthors, 2020: Small-scale structure of thermodynamic phase in Arctic mixed-phase clouds observed by airborne remote sensing during a cold air outbreak and a warm air advection event. *Atmos. Chem. Phys.*, **20** (9), 5487–5511, <https://doi.org/10.5194/acp-20-5487-2020>.
- Rutz, J. J., and Coauthors, 2019: The Atmospheric River Tracking Method Intercomparison Project (ARTMIP): Quantifying Uncertainties in Atmospheric River Climatology. *J. Geophys. Res. Atmospheres*, **124** (24), 13 777–13 802, <https://doi.org/10.1029/2019JD030936>.
- Sand, M., and Coauthors, 2017: Aerosols at the poles: An AeroCom Phase II multi-model evaluation. *Atmos. Chem. Phys.*, **17** (19), 12 197–12 218, <https://www.atmos-chem-phys.net/17/12197/2017/>.
- Scarlat, R. C., G. Heygster, and L. T. Pedersen, 2017: Experiences with an optimal estimation algorithm for surface and atmospheric parameter retrieval from passive microwave data in the Arctic. *IEEE J. Appl. Earth Obs. Rem. Sens.*, **10** (9), 3934–3947, <https://doi.org/10.1109/JSTARS.2017.2739858>.
- Scarlat, R. C., G. Spreen, G. Heygster, M. Huntemann, C. Pațilea, L. T. Pedersen, and R. Saldo, 2020: Sea ice and atmospheric parameter retrieval from satellite microwave radiometers: Synergy of AMSR2 and SMOS compared with the CIMR candidate mission. *J. Geophys. Res. Oceans*, **125** (3), e2019JC015 749, <https://doi.org/10.1029/2019JC015749>.
- Schacht, J., and Coauthors, 2019: The importance of the representation of air pollution emissions for the modeled distribution and radiative effects of black carbon in the Arctic. *Atmos. Chem. Phys.*, **2019**, 1–39, <https://doi.org/10.5194/acp-2019-71>.

- Schemann, V., and K. Ebell, 2020: Simulation of mixed-phase clouds with the ICON-LEM in the complex Arctic environment around Ny-Ålesund. *Atmos. Chem. Phys.*, **20**, 475–485, <https://doi.org/10.5194/acp-20-475-2020>.
- Schmale, J., P. Zieger, and A. M. L. Ekman, 2021: Aerosols in current and future Arctic climate. *Nature Climate Change*, **11** (2), 95–105, URL https://ideas.repec.org/a/nat/natcli/v11y2021i2d10.1038_s41558-020-00969-5.html, <https://doi.org/10.1038/s41558-020-00969-5>.
- Schneider, T., and Coauthors, 2022: Sensitivity to changes in the surface-layer turbulence parameterization for stable conditions in winter: A case study with a regional climate model over the Arctic. *Atmos. Sci. Lett.*, **23** (1), e1066, <https://doi.org/10.1002/asl.1066>.
- Schoger, S. Y., D. Moiseev, A. von Lerber, S. Crewell, and K. Ebell, 2021: Snowfall-rate retrieval for K- and W-Band radar measurements designed in Hyytiälä, Finland, and tested at Ny-Ålesund, Svalbard, Norway. *J. Appl. Meteorol. Clim.*, **60** (3), 273 – 289, <https://doi.org/10.1175/JAMC-D-20-0095.1>.
- Schulz, H., and Coauthors, 2019: High-Arctic aircraft measurements characterising black carbon vertical variability in spring and summer. *Atmos. Chem. Phys.*, **19** (4), 2361–2384, <https://doi.org/10.5194/acp-19-2361-2019>.
- Screen, J. A., 2021: An ice-free Arctic: What could it mean for European weather? *Weather*, **76** (10), 327–328, <https://doi.org/10.1002/wea.4069>.
- Screen, J. A., and I. Simmonds, 2010: The central role of diminishing sea ice in recent Arctic temperature amplification. *Nature*, **464**, 1334–1337, <https://doi.org/10.1038/nature09051>.
- Sedlar, J., and Coauthors, 2020: Confronting Arctic troposphere, clouds, and surface energy budget representations in regional climate models with observations. *J. Geophys. Res. Atmos.*, **125** (6), e2019JD031 783, <https://doi.org/10.1029/2019JD031783>.
- Sellers, W. D., 1969: A global climatic model based on the energy balance of the Earth-atmosphere system. *J. Appl. Meteorol.*, **8**, 392–400, [https://doi.org/10.1175/1520-0450\(1969\)008<0392:AGCMBO>2.0.CO;2](https://doi.org/10.1175/1520-0450(1969)008<0392:AGCMBO>2.0.CO;2).

- Seo, S., A. Richter, A.-M. Blechschmidt, I. Bougoudis, and J. P. Burrows, 2019: First high resolution BrO column retrievals from TROPOMI. *Atmos. Meas. Tech.*, <https://doi.org/10.5194/amt-12-2913-2019>.
- Serreze, M. C., and R. C. Barry, 2011: Processes and impacts of Arctic Amplification: A research synthesis. *Global Planet. Change*, **77**, 85–96, <https://doi.org/10.1016/j.gloplacha.2011.03.004>.
- Serreze, M. C., and J. A. Francis, 2006: The Arctic Amplification debate. *Clim. Change*, **76**, 241–264, <https://doi.org/10.1007/s10584-005-9017-y>.
- Shupe, M. D., and J. M. Intrieri, 2004: Cloud radiative forcing of the Arctic surface: The influence of cloud properties, surface albedo, and solar zenith angle. *J. Clim.*, **17** (3), 616–628, [https://doi.org/10.1175/1520-0442\(2004\)017<0616:CRFOTA>2.0.CO;2](https://doi.org/10.1175/1520-0442(2004)017<0616:CRFOTA>2.0.CO;2).
- Shupe, M. D., and Coauthors, 2022: Overview of the MOSAiC expedition: Atmosphere. *Elem. Sci. Anth.*, **10** (1), <https://doi.org/10.1525/elementa.2021.00060>.
- Smith, D. M., and Coauthors, 2019: The Polar Amplification Model Intercomparison Project (PAMIP) contribution to CMIP6: Investigating the causes and consequences of polar amplification. *Geosci. Model Dev.*, **12** (3), 1139–1164, <https://doi.org/10.5194/gmd-12-1139-2019>.
- Smith, D. M., and Coauthors, 2022: Robust but weak winter atmospheric circulation response to future Arctic sea ice loss. *Nat. Commun.*, **13**, 727, <https://doi.org/10.1038/s41467-022-28283-y>.
- Soppa, M. A., and Coauthors, 2019: Assessing the influence of water constituents on the radiative heating of Laptev Sea shelf waters. *Front. Mar. Sci.*, **6**, 221, <https://doi.org/10.3389/fmars.2019.00221>.
- Spren, G., L. de Steur, D. Divine, S. Geland, E. Hansen, and R. Kwok, 2020: Arctic sea ice volume export through Fram Strait from 1992 to 2014. *J. Geophys. Res. Oceans*, **125** (6), e2019JC016039, <https://doi.org/10.1029/2019JC016039>.
- Spren, G., S. Kern, D. Stammer, and E. Hansen, 2009: Fram Strait sea ice volume export estimated between 2003 and 2008 from satellite data. *Geophys. Res. Lett.*, **36** (19), L19502, <https://doi.org/10.1029/2009GL039591>.

- Stapf, J., 2021: Influence of Surface and Atmospheric Thermodynamic Properties on the Cloud Radiative Forcing and Radiative Energy Budget in the Arctic. Ph.D. thesis, 132 pp., Leipzig University.
- Stapf, J., A. Ehrlich, E. Jäkel, C. Lüpkes, and M. Wendisch, 2020: Reassessment of shortwave surface cloud radiative forcing in the Arctic: Consideration of surface-albedo–cloud interactions. *Atmos. Chem. Phys.*, **20** (16), 9895–9914, <https://doi.org/10.5194/acp-20-9895-2020>.
- Stapf, J., A. Ehrlich, and M. Wendisch, 2021: Influence of thermodynamic state changes on surface cloud radiative forcing in the Arctic: A comparison of two approaches using data from AFLUX and SHEBA. *J. Geophys. Res. Atmos.*, **126** (5), e2020JD033 589, <https://doi.org/10.1029/2020JD033589>.
- Steele, M., and T. Boyd, 1998: Retreat of the cold halocline layer in the Arctic Ocean. *J. Geophys. Res. Oceans*, **103** (C5), 10 419–10 435, <http://dx.doi.org/10.1029/98JC00580>.
- Stramler, K., A. Del Genio, and W. B. Rossow, 2011: Synoptically driven Arctic winter states. *J. Climate*, **47**, 1747–1762, <https://doi.org/10.1175/2010JCLI3817.1>.
- Sun, B., E. Jäkel, M. Schäfer, and M. Wendisch, 2020: A biased sampling approach to accelerate backward Monte Carlo atmospheric radiative transfer simulations and its application to Arctic heterogeneous cloud and surface conditions. *J. Quant. Spectrosc. Radiat. Transfer*, **240**, 106 690, <https://doi.org/10.1016/j.jqsrt.2019.106690>.
- Tan, I., G. Sotiropoulou, P. C. Taylor, L. Zamora, and M. Wendisch, 2021: A review of the factors influencing Arctic mixed-phase clouds: Progress and outlook. *Earth and Space Science Open Archive*, 54, <https://doi.org/10.1002/essoar.10508308.1>.
- Taylor, P. C., M. Cai, A. Hu, J. Meehl, W. Washington, and G. J. Zhang, 2013: A decomposition of feedback contributions to polar warming amplification. *J. Clim.*, **26**, 7023–7043, <https://doi.org/10.1175/JCLI-D-12-00696.1>.
- Thoman, R. L., J. Richter-Menge, and M. L. Druckenmiller, 2020: Arctic Report Card 2020. <https://doi.org/10.25923/mn5p-t549>.

- Triana-Gómez, A. M., G. Heygster, C. Melsheimer, G. Spreen, M. Negusini, and B. H. Petkov, 2020: Improved water vapour retrieval from AMSU-B and MHS in the Arctic. *Atmos. Meas. Tech.*, **13** (7), 3697–3715, <https://doi.org/10.5194/amt-13-3697-2020>.
- Triana-Gómez, A. M., A. M., G. Heygster, C. Melsheimer, and G. Spreen, 2018: Towards a merged total water vapour retrieval from AMSU-B and AMSR-E data in the Arctic Region. *IGARSS 2018-2018 IEEE International Geoscience and Remote Sensing Symposium*, IEEE, 1818–1821, <https://doi.org/10.1109/IGARSS.2018.8517863>.
- Tsubouchi, T., K. Våge, B. Hansen, K. M. H. Larsen, S. Österhus, C. Johnson, S. Jónsson, and H. Valdimarsson, 2021: Increased ocean heat transport into the Nordic Seas and Arctic Ocean over the period 1993–2016. *Nat. Clim. Change*, **11**, 21–26, <https://doi.org/10.1038/s41558-020-00941-3>.
- Uttal, T., and Coauthors, 2002: Surface heat budget of the Arctic Ocean. *Bull. Am. Meteorol. Soc.*, **83**, 255–275, [https://doi.org/10.1175/1520-0477\(2002\)083<0255:SHBOTA>2.3.CO;2](https://doi.org/10.1175/1520-0477(2002)083<0255:SHBOTA>2.3.CO;2).
- Viceto, C., I. V. Gorodetskaya, A. Rinke, M. Maturilli, A. Rocha, and S. Crewell, 2022: Atmospheric rivers and associated precipitation patterns during the ACLOUD and PASCAL campaigns near Svalbard (May–June 2017): case studies using observations, reanalyses, and a regional climate model. *Atmos. Chem. Phys.*, **22**, 441–463, <https://doi.org/10.5194/acp-22-441-2022>.
- von Lerber, A., M. Mech, A. Rinke, D. Zhang, M. Lauer, A. Radovan, I. Gorodetskaya, and S. Crewell, 2022: Evaluating seasonal and regional distribution of snowfall in regional climate model simulations in the Arctic. *Atmos. Chem. Phys.*, **22**, 7287–7317, <https://doi.org/10.5194/acp-22-7287-2022>.
- Walbröl, A., and Coauthors, 2022: Atmospheric temperature, water vapour and liquid water path from two microwave radiometers during MOSAiC. *Scientific Data*, **accepted**.
- Warren, S. G., and W. J. Wiscombe, 1980: A model for the spectral albedo of snow. II: Snow containing atmospheric aerosols. *J. Atmos. Sci.*, **37**, 2734–2745, [https://doi.org/10.1175/1520-0469\(1980\)037<2734:AMFTSA>2.0.CO;2](https://doi.org/10.1175/1520-0469(1980)037<2734:AMFTSA>2.0.CO;2).

- Wendisch, M., D. Handorf, I. Tegen, R. A. J. Neggers, and G. Spreen, 2021: Glimpsing the ins and outs of the Arctic atmospheric cauldron. *Eos*, <https://doi.org/10.1029/2021EO155959>.
- Wendisch, M., and Coauthors, 2017: Understanding causes and effects of rapid warming in the Arctic. *Eos*, **98** (8), 22–26, <https://doi.org/10.1029/2017EO064803>.
- Wendisch, M., and Coauthors, 2019: The Arctic cloud puzzle: Using ACLOUD/PASCAL multi-platform observations to unravel the role of clouds and aerosol particles in Arctic amplification. *Bull. Am. Meteorol. Soc.*, **100** (5), 841–871, <https://doi.org/10.1175/BAMS-D-18-0072.1>.
- Wesche, C., D. Steinhage, and U. Nixdorf, 2016: Polar aircraft Polar 5 and Polar 6 operated by the Alfred Wegener Institute. *J. Large-Scale Res. Facilities*, <https://doi.org/10.17815/jlsrf-2-153>.
- Wex, H., and Coauthors, 2019: Annual variability of ice nucleating particle concentrations at different Arctic locations. *Atmos. Chem. Phys.*, **19**, 5293–5311, <https://doi.org/10.5194/acp-19-5293-2019>.
- Wille, J. D., and Coauthors, 2021: Antarctic atmospheric river climatology and precipitation impacts. *J. Geophys. Res. Atmos.*, **126** (8), e2020JD033788, <https://doi.org/10.1029/2020JD033788>.
- Willis, M. D., and Coauthors, 2019: Aircraft-based measurements of high Arctic springtime aerosol show evidence for vertically varying sources, transport and composition. *Atmos. Chem. Phys.*, **19** (1), 57–76, <https://doi.org/10.5194/acp-19-57-2019>.
- Wohlmann, I., R. Lehmann, and M. Rex, 2017: Update of the Polar SWIFT model for polar stratospheric ozone loss (Polar SWIFT version 2). *Geosci. Model Dev.*, **10**, 2671–2689, <https://doi.org/10.5194/gmd-10-2671-2017>.
- Xi, H., and Coauthors, 2021: Global chlorophyll a concentrations of phytoplankton functional types with detailed uncertainty assessment using multi-sensor ocean color and sea surface temperature satellite products. *J. Geophys. Res. Oceans*, **126**, e2020JC017127, <https://doi.org/10.1029/2020JC017127>.
- Yang, P., L. Bi, B. A. Baum, K.-N. Liou, G. W. Kattawar, M. I. Mishchenko, and B. Cole, 2013: Spectrally consistent scattering, absorption, and polarization properties of atmospheric

- ice crystals at wavelengths from 0.2 to 100 μ m. *J. Atmos. Sci.*, **70** (1), 330–347, <https://doi.org/10.1175/jas-d-12-039.1>.
- Zahn, M., M. Akperov, A. Rinke, F. Feser, and I. I. Mokhov, 2018: Trends of cyclone characteristics in the Arctic and their patterns from different reanalysis data. *J. Geophys. Res. Atmos.*, **123** (5), 2737–2751, <https://doi.org/10.1002/2017JD027439>.
- Zanatta, M., A. Herber, Z. Jurányi, O. Eppers, J. Schneider, and J. P. Schwarz, 2021: Technical note: Sea salt interference with black carbon quantification in snow samples using the single particle soot photometer. *Atmos. Chem. Phys.*, **21** (12), 9329–9342, <https://doi.org/10.5194/acp-21-9329-2021>.
- Zanatta, M., and Coauthors, 2018: Effects of mixing state on optical and radiative properties of black carbon in the European Arctic. *Atmos. Chem. Phys.*, **18**, 14 037–14 057, <https://doi.org/10.5194/acp-18-14037-2018>.
- Zeppenfeld, S., M. van Pinxteren, A. Engel, and H. Herrmann, 2020: A protocol for quantifying mono- and polysaccharides in seawater and related saline matrices by electro-dialysis (ED) – combined with HPAEC-PAD. *Ocean Sci.*, **16** (4), 817–830, <https://doi.org/10.5194/os-16-817-2020>.
- Zeppenfeld, S., M. van Pinxteren, M. Hartmann, A. Bracher, F. Stratmann, and H. Herrmann, 2019: Glucose as a potential chemical marker for ice nucleating activity in Arctic seawater samples. *Environ. Sci. Technol.*, **53** (15), 8747–8756, <https://doi.org/10.1021/acs.est.9b01469>.
- Zhang, Z., H. Bi, K. Sun, H. Huang, Y. Liu, and L. Yan, 2017: Arctic sea ice volume export through the Fram Strait from combined satellite and model data: 1979–2012. *Acta Oceanol. Sin.*, **36**, 44–55, <https://doi.org/10.1007/s13131-017-0992-4>.